

AMERICAN UNIVERSITY OF BEIRUT

BIODEGRADABLE, INKJET-PRINTED NEURAL INTERFACE

by
REEM MOUNZER ALMASRI

A thesis
submitted in partial fulfillment of the requirements
for the degree of Master of Science
to the Biomedical Engineering Program
of the Maroun Semaan Faculty Engineering and Architecture and Faculty of Medicine
at the American University of Beirut


Beirut, Lebanon
September 2019

AMERICAN UNIVERSITY OF BEIRUT


BIODEGRADABLE, INKJET-PRINTED NEURAL INTERFACE

by
REEM MOUNZER ALMASRI


Approved by:


Prof. Massoud Khraiche, Assistant Professor
Biomedical Engineering

Advisor


Prof. Lyne Bilston, Professor
Clinical School Operating

Member of Committee


Prof. Jason Amaloury, Assistant Professor
Biomedical Engineering

Member of Committee


Prof. Ali Tehrani, Assistant Professor
Chemical Engineering and Advanced Energy

Member of Committee

Date of thesis defense: September 11, 2019

AMERICAN UNIVERSITY OF BEIRUT

THESIS, DISSERTATION, PROJECT RELEASE FORM

Student Name:

Almasri _____ Reem _____ Mounzer _____
Last First Middle

Master's Thesis Master's Project Doctoral Dissertation

I authorize the American University of Beirut to: (a) reproduce hard or electronic copies of my thesis, dissertation, or project; (b) include such copies in the archives and digital repositories of the University; and (c) make freely available such copies to third parties for research or educational purposes.

I authorize the American University of Beirut, to: (a) reproduce hard or electronic copies of it; (b) include such copies in the archives and digital repositories of the University; and (c) make freely available such copies to third parties for research or educational purposes after:

One ---- year from the date of submission of my thesis, dissertation, or project.

Two ---- years from the date of submission of my thesis, dissertation, or project.

Three ✓ years from the date of submission of my thesis, dissertation, or project.

Signature



Date

September 24, 2019

This form is signed when submitting the thesis, dissertation, or project to the University Libraries

ACKNOWLEDGMENTS

Firstly, I would like to thank everyone who had contributed to the successful completion of this thesis. My recognition and gratitude are addressed to my advisor, Prof. Massoud Khraiche for his guidance, support and his enormous patience throughout the development of the work. Besides my advisor, I would like to thank all my committee members for the insightful comments and helpful feedback. Special thanks to Prof. Ali Tehrani for his continuous guidance and for opening his lab to me all the time.

In addition, I would also like to express my gratitude to my loving parents and friends who had helped and given me encouragement. Moreover, special thanks to my lab colleagues, especially Rima El-Hassan and Walid Al-Chamaa, for the stimulating discussions, and the sleepless nights that we spent working together.

AN ABSTRACT OF THE THESIS OF

Reem Mounzer Almasri for Master of Science
Major: Biomedical Engineering

Title: Biodegradable, Inkjet-printed Neural Interface

The evolution of the neural prosthesis as a clinical solution holds significant promise for treatment and management of neurological disorders such as Parkinson's, Alzheimer's and Epilepsy. In this work, we developed and built a new generation of biodegradable and flexible neural interfaces that have the potential to record high-fidelity electrical activity from the brain for monitoring neurological diseases and guiding therapeutic decisions without the need for prosthetic device resection. For that purpose, we utilized innovations in inkjet printing technology aimed at overcoming limitations of current semiconductor fabrication techniques on low melting point polymer substrates. Inkjet printing allows for the fabrication of electronic devices at a resolution of a few tens of microns with reduced material waste, low cost and low temperatures. The devices in this study were fabricated on flexible polymers that allow for reduced mechanical mismatch between soft brain tissue and implanted devices improving the biocompatibility of prosthetic intervention. The devices were fabricated on polycaprolactone (PCL), a biodegradable polyester with a low melting point of around 60 °C and polyimide (PI) a low moisture uptake and biocompatible polymer. Electrodes for neural recording were built at 50 μm diameter using (3,4- ethylenedioxythiophene)-poly(styrenesulfonate) (PEDOT:PSS). The latter is a low impedance organic semiconductor and it was deposited in 10 layers via non-contact inkjet printing reducing the impedance to $\sim 200 \Omega$ at 1 KHz leading to increased electrical and ionic conductivities. In-vitro validation was performed on both rat PC12 cells and isolated neural rat retina to confirm their biocompatibility of the fabricated devices and their ability to record single unit activity from spontaneously firing neurons. The study shows the potential of inkjet printing for building high performance, biodegradable and flexible neural interfaces.

CONTENTS

ACKNOWLEDGEMENTS.....	v
ABSTRACT.....	vi
LIST OF ILLUSTRATIONS.....	ix
LIST OF TABLES.....	xii
LIST OF ABBREVIATIONS.....	xiii
Chapter	
1. INTRODUCTION.....	1
2. LITERATURE REVIEW.....	3
2.1. Neuron-Electrode Interface.....	3
2.2. Challenges in Neural Recording.....	5
2.3. Advancements in Electrode Structures and Coatings.....	6
2.4. Nanoparticles in the Biomedical Field.....	7
2.5. Biodegradable Materials for Neural Prosthetics.....	8
2.6. Mechanical Properties of Neural Implants.....	11
2.7. Material Jetting Technology.....	13
2.7.1 Jetting Waveform.....	15
2.7.2 Electability Assessment.....	16
3. SPECIFIC AIMS.....	18
4. METHODOLOGY.....	20

5. RESULTS	36
5.1. Surface Characterization.....	38
5.2. Mechanical Testing.....	40
5.3. Electrochemical Characterization.....	44
5.4. Ag Ink Sintering.....	49
5.5. Physiological Recordings.....	52
5.6. Biocompatibility.....	54
5.7. Degradation Test.....	56
6. DISCUSSION	58
7. CONCLUSION	62
BIBLIOGRAPHY	64

ILLUSTRATIONS

Figure		Page
1.	Circuit model of neuron-electrode interface.....	4
2.	Weight loss (%) and density degradation of PCL in vivo for a period of 130 weeks	11
3.	A typical fabrication process of microelectrodes.....	13
4.	A) 1 pL nozzles in a 16-jet Dimatix Materials Cartridge. B) A line with a certain length can consist of more or less drops according to resolution (drop spacing).....	14
5.	Schematic diagram of the print head with stages of jetting for a basic waveform.....	16
6.	An example of droplet formation states taken via drop watcher camera for the PVPh ink.....	22
7.	Chemical structures of A) PVPh, B) PMF, C) Crosslinked PVPh+PMF, D) PEDOT:PSS, E) PCL, F) PLGA, G) CS.....	23
8.	Fabrication process of Ag/PEDOT:PSS electrodes (a to e) on PI and (f to j) on PCL.....	28
9.	Top view of the electrode patterns.....	29
10.	Schematic illustration of NPs' sintering process.....	30
11.	Schematic of consecutive light pulses with 1 ms pulse width.....	31
12.	A) Schematic diagram of a four-point probe circuit, B) Four-point probe system (Ossila).....	31
13.	The general recording setup for the electrophysiological activity of the retina.....	33

14.	A) A 16-electrode biodegradable neural interface printed on PCL. B, C) Closeup of Ag-nanoparticles electrode leads printed with 100 μm line width on PCL. D) Closeup of recording sites where Ag-nanoparticles leads terminate with PEDOT:PSS electrodes of 70 μm . The leads are passivated with PCL. E) A 16-electrode neural interface printed on PI. F, G) Closeup of Ag-nanoparticles electrode leads printed with 50 μm line width on PCL. D) Closeup of recording electrode where Ag-nanoparticles lead terminate with PEDOT:PSS-coated electrode of 50 μm . The leads are passivated with PVPh.....	36
15.	Raman spectrum of thermally treated PEDOT:PSS films at 90 $^{\circ}\text{C}$ for 3 hours.....	37
16.	SEM images for the surfaces of A) CS, B) PCL, C) PLGA, and D) PI. All scale bars indicate 200 μm	38
17.	AFM images of PI plasma-treated substrates: A) no treatment, B) 10 minutes etching, and C) 30 minutes etching.....	39
18.	The distribution of stress in the PCL microelectrode array with a thickness of 13 μm at the fracture critical state.....	42
19.	Stress-strain analysis of A) PCL vs. PI, B) PI vs. PI/PVPh, and D) PCL vs. PCL/PLGA. C) Microphotographic photos for soft conformal PCL-based array showing 4 electrodes lying on the surface of rat brain E) Schematic scaling that shows the mechanical properties of the brain tissue and utilized polymers.....	43
20.	Impedance magnitude at 1 kHz on 50 μm electrodes.....	45
21.	A) EIS shows impact of PEDOT:PSS multiple layer printing on 50 μm electrode impedance (lower impedance results in lower recording noise). D) EIS shows impact of PEDOT:PSS electrode diameter on electrode impedance. B, E, C, F) Figures show the impact of number of PEDOT:PSS layers and electrode diameter on CSC, data essential to evaluate the amount of charge delivered by electrodes.....	47
22.	A) EIS shows the difference in impedance between 50 μm electrodes printed on PI vs. PCL. B) CV responses for 50 μm electrodes printed on PI vs. PCL. C) EIS shows the impact of coating material on 50 μm electrode impedance (lower impedance with graphene/PEDOT:PSS coating). D) CV shows the impact of coating material on 50 μm electrode CSC (higher CSC with graphene/PEDOT:PSS coating).....	48

23.	Microscopic and SEM images of typical Ag patterns on A) PCL and B) PI after flashing two times. SEM images show the morphology changes on the surface on the electrodes after treatment. Scale bars indicate 200 μm	50
24.	The relationship between electrical resistance and the number of light pulses for inkjet-printed Ag patterns on to PI and PCL substrates.....	51
25.	SEM images for Ag nanoparticles: A) before sintering, B) after thermal sintering, and C) after light sintering. The scale bars indicate 100 nm, 250 nm, and 250 nm respectively.....	51
26.	A) A printed array showing 8 electrodes with different diameters ranged between 50 μm to 100 μm . B) Closeup of the recording setup where the array in (A) is connected to the ME2100 system via zifboard. C) Three single-units activity recorded by electrodes array and detected by spike sorter.....	52
27.	Post stimulus time histogram (PSTH) of a rat retinal ganglion cell response to a light stimulus.....	53
28.	Photomicrographs depicting morphology of adherent PC12 cells on: A) PI substrate, B) PCL substrate, and D) TCP (control). C) Electrode surrounded by PC12 cells on PCL substrate.....	55
29.	The percentage of viable cells in total cell population on PI substrate, PCL substrate, and tissue culture plastic.....	55
30.	Images collected at several stages of accelerated dissolution of interfaces immersed into an aqueous buffer solution (pH 13) at 37 °C. A) for PCL, and B) for PCL/PLGA.....	57

TABLES

Table		Page
4.1.	Physical properties and printing indicator of the prepared inks at room temperature.....	23
4.2.	Inkjet printing parameters for the deposition of the inks.....	24
5.1.	Average of contact angles and widths of lines inkjet printed on plasma treated PI films.....	40
5.2.	Resistance of printed Ag patterns on PCL	49

ABBREVIATIONS

AFM	Atomic force microscope
ASTM	American Society for Testing and Materials
CPs	Conductive polymers
CS	Chitosan
CSC	Charge storage capacity
CSF	Cerebrospinal fluid
CV	Cyclic voltammetry
DMEM	Dulbecco's Modified Eagle's Medium
DMF	Dimethylformamide
DMSO	Dimethyl sulfoxide
DOD	Drop-on-demand
ECoG	Electrocorticography
EIS	Electrochemical impedance spectroscopy
FBS	Fetal bovine serum
FDA	Food and Drug Administration
MEAs	Multi-electrode arrays
NPs	Nanoparticles
PBS	Phosphate buffer saline
PCL	Poly(caprolactone)
PDMS	Poly-di-methyl-siloxane
PDS	Poly(dioxanone)
PEDOT:PSS (styrenesulfonate)	Poly(3,4-ethylenedioxythiophene)poly
PGA	Polyglycolide, Poly glycolic acid
PI	Polyimide
PLA	Poly lactic acid
PLGA	Poly(lactide-co-glycolide)
PMF	Poly(melamine-co-formaldehyde)
PPy	Poly-pyrrole
PSTH	Post Stimulus Time Histogram
Pt	Platinum
PVPh	Poly(4-vinylphenol)
SEM	Scanning electron microscope
SNR	Signal to noise ratio
TB	Trypan Blue
TCP	Tissue culture plastic

CHAPTER 1

INTRODUCTION

The heterogenous groups of neural degenerative diseases manifest in progressive damage to neurons, neural connections and neural networks and they include Parkinson's, a progressive disorder of the nervous system that affects movement; epilepsy, a disorder in which nerve cell activity in the brain is disturbed, causing seizures; Alzheimer's, a progressive disease that destroys memory, and other important cognitive functions and causes motor cortex deficits; depression, a mood disorder causing a persistent feeling of sadness and loss of interest; blindness, loss of vision due to complications with the retina and optic nerve [2]. The neural prostheses have emerged as effective and clinically viable treatment for several neural degenerative diseases. This technology manipulates the electrophysiological signals in the neural tissue via an implantable device. Some devices have stimulation and recording functions integrated into the same interface. This class of devices aims at repairing or bridging damaged neural pathways or substituting for lost motor, sensory or cognitive modalities, while the other part of the device aims at recording the neural activity synchronously to check the efficiency of stimulation on the targeted neurons. Nowadays, the evolution of such devices as a clinical solution for the treatment and management of these neurological disorders has been focused on reducing tissue damage, increasing stimulation/recording resolution, and prolonging implant life [3]. Given the complexity of the chronic integration of an electronic device with neural tissue, many approaches and technologies have been used to improve prosthetic intervention. For example, many engineering efforts have focused on utilizing different

types of materials to enhance the neural prosthetics' performance including polymers. This type of materials can exhibit tremendous flexibility and conformality that can mimic the neural tissue properties and withstand the surrounding environment. Moreover, using biodegradable and biocompatible polymers as backbones, can considerably reduce tissue infection and undesired responses, as well as negates the risk associated with the additional surgical procedure and potential damage to vital neural tissue during device resection.

CHAPTER 2

LITERATURE REVIEW

The objective of this literature survey is to give a general overview about some important concepts related to the thesis work. An overview of the circuit model that defines the neuron-electrode interface, including some tailoring methods to enhance the electrode's performance are given. In addition, the use of biodegradable materials as a main part of the interface is deliberated as well as the mechanical properties of the interface. Finally, jetting technology and the properties that controls the fabrication process of the devices are discussed.

2.1 Neuron-Electrode Interface

The neural-electrode interface is represented by a circuit model that serves as a powerful tool to better understand the physiological interactions as shown in figure 1. In this model, basic circuit elements, like resistors and capacitors, are used to represent the factors that evaluate the electrical characteristics of the neural interface. These components include double layer impedance (Z_{CPE}), charge transfer resistance (R_{ct}), Warburg element (Z_W), and solution resistance (R_S). The latter is defined as the resistance between the working electrode and the reference electrode in an ionic solution. This factor is mostly dominated by the geometrical area of the electrode and the ionic concentration in solution. R_S is inversely proportional to the size of the electrode as described in the equation: $R_S = \frac{\rho}{4r}$; where, ρ is the solution resistivity and r is the radius of the electrode. R_{ct} is the resistivity of the electron transferring from the electrode to the solution. Similarly, the size of the electrode and the active surface area of the electrode which is in

contact with the solution are important parameters that affect R_{ct} . The diffusion impedance or Warburg element is generated from the diffusion process of ionic species at the interface. Generally, the impedance is expressed as a function of frequency. At low frequencies, the capacitive behavior of the electrode's material dominates the interaction as the ions and reactants diffuse far from the electrode surface, leading to high impedances. However, the impedance decreases at higher frequencies because the reactants become unable to move far from the electrode's surface. The common standard way to measure diffusion impedances is through electrochemical impedance spectroscopy (EIS). Double layer impedance is created when two sheets of opposite charges form at the electrode surface and electrolyte, making an additional capacitive effect. A high impedance value causes high thermal noise which leads to lower signal to noise ratio. The size of the electrode plays an important role in changing the electrode performance, since increasing the surface area reduces the impedance, but at the expense of spatial resolution. Finally, depositing coating materials on the surface of the electrode creates an additional layer to the electrode that is modeled by a capacitor (C_C). However, as the conductivity of the CP increases, the dielectric effect decreases.

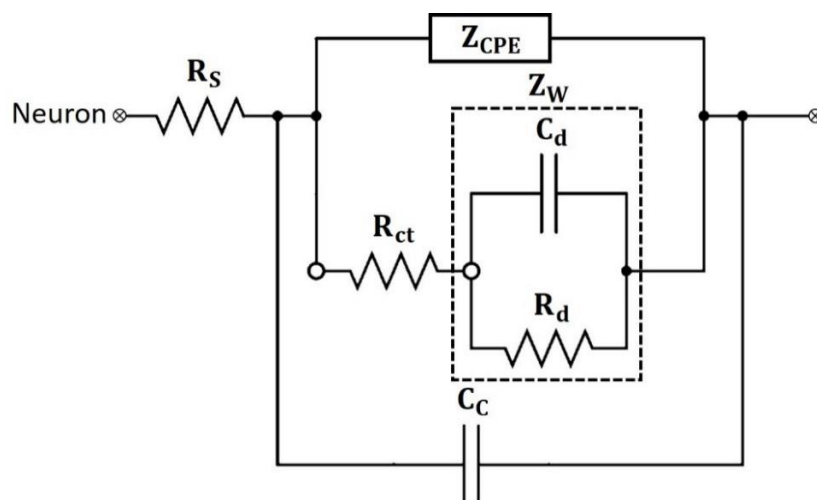


Figure 1. Circuit model of neuron-electrode interface

2.2 Challenges in Neural Recording

Understanding the neuronal behaviors and their physiological functions require tools that can probe and bridge the signaling complexity of the neural networks. One fundamental step in approaching this sophisticated interface is to use recording electrodes that mainly serve in numerous applications including brain-machine interface for neuro-prosthetics and clinical therapies for neurological disorders (Parkinson, Epilepsy, etc). Accordingly, it is essential to increase the neuron/electrode coupling conditions and subsequently enhance the signal quality. There are two main types of neuronal recording: intracellular and extracellular. The traditional intracellular recordings use an invasive technique that penetrate the cell membrane, known as patch clamp [4]. This technique relies on forming a direct contact between the electrode and cytosol by breaking-off of the cell's plasma membrane and connecting it to a hollow glass tube known as a micropipette [4]. The use of patch microelectrodes for recording is practically limited as their mechanical stability decreases with time causing damage to the plasma membrane and disturbance of the intracellular ionic contents [5]. In addition, such intimate access demands a large clinical setup which restricts the feasibility of this method on freely behaving agents and disturbs the cell viability leading to short-duration measurements [6]. Accordingly, in order to overcome these drawbacks, extracellular recording techniques, such as multi-electrode arrays (MEAs), are used. MEAs provide large-scale and long-term measurements of excitable cells at the expense of low signal resolution whether in strength or quality [7, 8]. In other words, these electrodes experience significant difficulties in determining the origin of the signal, as they are blind to sub-threshold synaptic potentials generated by individual neurons. Therefore, the need to

modify the design of planar MEAs was realized by focusing on optimizing the neuron-electrode interface.

2.3 Advancements in Electrode Structures and Coatings

Tailoring the electrode by modifying its material properties or geometrical structure can enhance the signal quality. Recent studies suggest that the electrode performance can be significantly improved by optimizing the electrode's effective surface area, while maintaining its small size [9, 10]. In other words, the topography of the electrode can be manipulated by fabricating micro/nano protrusions on its surface such as nanowires and nanotubes to increase the effective surface area. Others used these 3D structures to direct the neurons toward engulfing them by active mechanisms, thus enhancing cell recordings and network formation.

The second way to reduce the impedance effect is by depositing additional biocompatible materials that are capable of adding electrochemical and topographical means to the electrode. Attention has been drawn lately to the use of conductive polymers (CPs), such as poly-pyrrole (PPy) and poly(3,4-ethylenedioxythiophene)-poly(styrenesulfonate) (PEDOT:PSS) [11, 12]. The latter is favorable and widely used due to its biocompatibility, stability, solution processability and electrical conductivity. Owing to the hydrophilic PSS segment, PEDOT can be easily dispersed in solutions. Having this material in aqueous form facilitates in low-cost solution coating and printing. It also allows for other solvents and surfactants, such as dimethylsulfoxide (DMSO) [13-15], dimethylformamide (DMF) [16], and TritonX [17, 18] to be added in order to manipulate the overall solution's chemical, mechanical, and electrical properties. Moreover, PEDOT:PSS enable mixed transport of both ions and electrons, making it very

suitable for bioelectronic applications. Owing to these unique properties, coating the electrode surface with PEDOT:PSS provides a significant increase in the electrode's electrochemical performance with both electronic and ionic currents are enabled [11]. This implies that the advantage of using such coating is proved by its long-term stability [19], enhanced SNR [20], and high charge storage capacity [21] in both recording and stimulation electrodes in comparison to other extensively used materials. Also, the enhanced interface biocompatibility of the electrode permits better cell adhesion and growth [22, 23]. Moreover, many studies have suggested using adhesion-promoting proteins like laminin-111 and fibronectin to increase the seal between the neuronal membrane and the electrode surface [24, 25].

2.4 Nanoparticles in the Biomedical Field

Nanoparticles (NPs) are nano-scaled materials that have unique properties and play important roles in multiple biomedical applications. NPs are categorized according to their synthesis method, surface functionalization, and type of application. In the past few years, NPs have been utilized in drug delivery [26, 27], bio-integrated devices [28, 29], electronics [30, 31], and consumer products [32]. Recently, many studies have been conducted to investigate the biocompatibility of these NPs especially in the applications that involve internal exposure (e.g. in the systemic circulation) [33]. There are many factors that determine the biological interactions of the NPs, including their size, shape, charge, and concentration [34-36]. These interactions may involve, cellular activation, cellular uptake as well as distribution in tissue. However, cytotoxicity happens only when the NPs induce cell death, abnormal cellular behavior, or an immune response. Many

studies concluded that large NPs are less likely to be taken up by the cells. In other words, as the size of the NPs increases, the toxic effects decrease [37, 38].

Metallic NPs, such as AuNPs and AgNPs, are widely used in the fabrication of electrical connections as they permit high conductivity and stability. As these NPs differ in their synthesis process, the ionic form of such metals might be released in the blood. AgNPs, for example, releases Ag⁺ ions, if they lose their stability during their functional lifespan. Ag⁺ ions are abundantly more toxic than AgNPs themselves, assuming equal molar concentration, as they are easily taken up by the cells [39]. On the other hand, a recent study mentioned that although these NPs are majorly taken up by the cells, their toxic effects are insignificant at low concentrations (≤ 25 mg/L) [36]. Despite the rapid advancement in the field of nanotechnology, in vivo experiments that investigate the biocompatibility of the NPs and the controlling mechanisms are still limited.

2.5 Biodegradable Materials for Neural Prosthetics

The use of biodegradable and biocompatible materials in current technology is an emerging area of research that aims at replacing and reducing the use of materials that cannot be broken down by natural processes. The American Society for Testing and Materials (ASTM) defines a biodegradable plastic as the following: "A plastic designed to undergo a significant change in its chemical structure under specific environmental conditions resulting in a change of properties that may vary as measured by standard test methods appropriate to the plastic and the application in a period of time that determines its classification, in which the degradation results from the action of micro-organisms occurring naturally". Some of these biodegradable materials are naturally originated such as chitosan (CS), agarose, collagen, alginate, and starch. Another group of these materials

consists of man-made polymers like poly(dioxanone) (PDS), polyglycolide (PGA), poly(caprolactone) (PCL), and polylactides (PLLA, PDLA). In the field of biomedical applications, utilizing such materials in implants reduces triggers of immune response, as well as inflammations associated with multiple surgeries. Biodegradable scaffolds, for instance, can serve as temporary supports that guide cell growth and tissue repair for a defined period [40, 41]. Also, these materials can serve as anti-inflammatory biomolecules, or as drug sources when degraded at the targeted tissue [42]. In addition, they can be fabricated to serve as substrates to hold electrodes for postoperative studies. The latter has various applications in the field of neuro-engineering especially in monitoring/modulating neural activity via electrodes. Almost all neural implants have a limited lifespan due to multiple mechanical and physiological challenges encountered by the hostile environment. In addition, in some applications, neural implants are required to function for a certain period of time. An example for such implants is electrocorticography (ECoG). This technology is being adopted to record the electrical activity from the brain to monitor, predict, and localize seizures. It uses surface electrodes placed over the exposed brain to record electrical activity from the cerebral cortex. Primarily, ECoG is applied for continuous examining of brain activity, that extends beyond pre-op to post-op monitoring of the patients. Not only ECoG, but also almost all neural implants require surgical intervention for their removal, which poses a risk for the patient with the additional surgical procedure and potential damage to vital neural tissue during device resection [2, 43]. Therefore, a wide variety of biodegradable and bioresorbable materials has been used in prosthetic devices for neural mapping experiments. A study has used tyrosine-derived polycarbonate polymers to fabricate a peripheral nerve interface with recording capabilities [44]. A more extensively studied

polymer is Poly(lactide-co-glycolide) (PLGA), which is a biocompatible and biodegradable polymer that is approved by the United States Food and Drug Administration (FDA). PLGA is a transparent synthetic copolymer composed of lactic acid (α -hydroxy propanoic acid) and glycolic acid (hydroxy acetic acid) which degrades in vitro through hydrolysis of ester bonds. The final degradation products in vitro are lactic acid and glycolic acid. The proportion of glycolic acid plays a role in determining the hydrophilicity and degradation rate of the overall polymer [45]. The degradation rate increases with higher glycolic acid content. A recent study has used PLGA as a temporary biodegradable substrate to record and monitor the neural activity; replacing the invasive ECoG [46].

PCL is another example of the most common biodegradable materials that can be used in biomedical applications. It is mainly a polyester that consists of ester linkages. The hydrolysis of these linkages initiates the degradation process, resulting in caproic acid as a byproduct. PCL has a significantly slow degradation rate that can be tailored, according to its size, molecular weight, degree of crystallinity, and morphology, in order to degrade within several months or even couple of years [47]. This enables it to be used in long-term applications, such as implantable devices and scaffolds. There are multiple in vivo studies that demonstrate the biodegradation of PCL [47-49]. Figure 2 shows in vivo degradation of PCL in rabbits for a period of 130 weeks [47]. Although it is not widely translated to clinical trials especially in the field of neural implants, PCL has been recently approved by FDA for the use in medical devices [50]. Usually PCL is used as a scaffold in tissue engineering applications [51, 52]. To our knowledge, there are some studies that used PCL-based electrodes to repair injured nerves by directed nerve regeneration [53, 54].

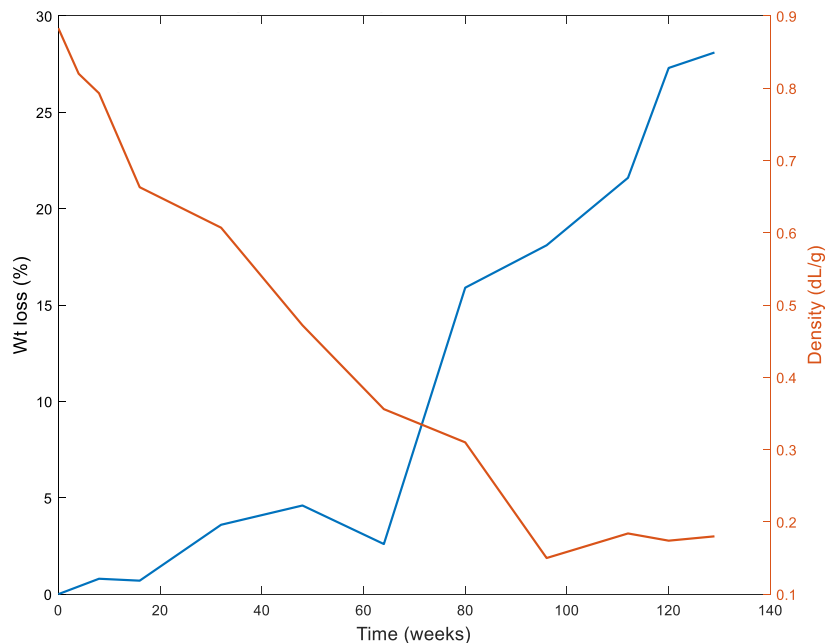


Figure 2. Weight loss (%) and density degradation of PCL in vivo for a period of 130 weeks

2.6 Mechanical Properties of Neural Implants

The success or failure of any neural implant is mainly determined by the interface between the technical device material and the soft brain tissue. One key technical challenge that encounters stiff implantable electrodes (e.g. silicon), is the mechanical mismatch at the interface [55, 56]. This issue is a potential source of scar formation, inflammation, immune response, and physical damage of the interface which eventually diminish the signal resolution in field of the targeted site and damage the surrounding tissue [57, 58]. One of the most effective solutions to this problem is to make the interface flexible and conformal to be able to handle the shear forces exhibited by repeatable micromotions of nearby tissues [59]. Such flexible interfaces can be achieved by either reducing the thickness of the substrate, therefore obtaining a smaller bending stiffness, or by utilizing soft materials to fabricate the device's backbone. In the latter case, there have been huge strides in the development of materials by getting advantage of their

outstanding properties to enhance the performance of neural interfaces. Although the current fabrication methods of prosthetic devices are focused on inorganic materials, many recent studies are concentrating on utilizing wide variety of organic materials for some structures or for the whole interface. In principle, the weak intermolecular forces in organic materials provide a high mechanical flexibility given that their young's modulus is comparable with neural tissue, which ranges in few hundreds of pascals ~350 Pa, and much smaller than that of inorganic materials [60, 61]. Polymers are the most common material class for neural implants, including the substrate and insulation of interconnection wires, as they exhibit optimal performance in terms of biocompatibility and flexibility. It has been shown that polymers function well when requirements of long-term stability in a hostile surroundings, and little response to implantation [60]. Soft polymers such as polyimide (PI) and poly-di-methyl-siloxane (PDMS) are widely used as flexible substrates in neural interfaces [60].

Polyimide, specifically, is known for its superior thermal and chemical resistance, excellent electrical and thermal insulation of metallic conductors, biocompatibility, and great elasticity. While maintaining its flexibility, PI can tolerate high temperatures up to 400 °C which permits a wide range of metals to be deposited during the fabrication process [62]. Chronic in vitro and in vivo studies have proved that the foreign body response evoked by implants made of PI is not significant whether in central or peripheral nervous system applications [63-66]. These devices functioned properly for months with high biostability and structural compatibility [67, 68].

2.7 Material Jetting Technology

Semiconductor fabrication techniques are the most well-established and most commonly used methods for microfabrication of functional neural interfaces. However, as the next generation of prosthetics aims to evolve into complex devices composed of heterogenous materials fabricated on a flexible low-melting point substrate, it would require more and more sophisticated semiconductor fabrications with more than hundreds of steps to build these devices. A very simple neural interface has to go through vacuum deposition, spin coating of photoresist layer, baking, photolithographic patterning, developing, etching, and stripping of the photoresist masking layer leading to an increase in the fabrication cost (Figure. 3). While flexible polymer backbones are thermally and chemically incompatible with resists, etchants and developers used in conventional microfabrication methods, other low-temperature fabrication technologies are evolved.

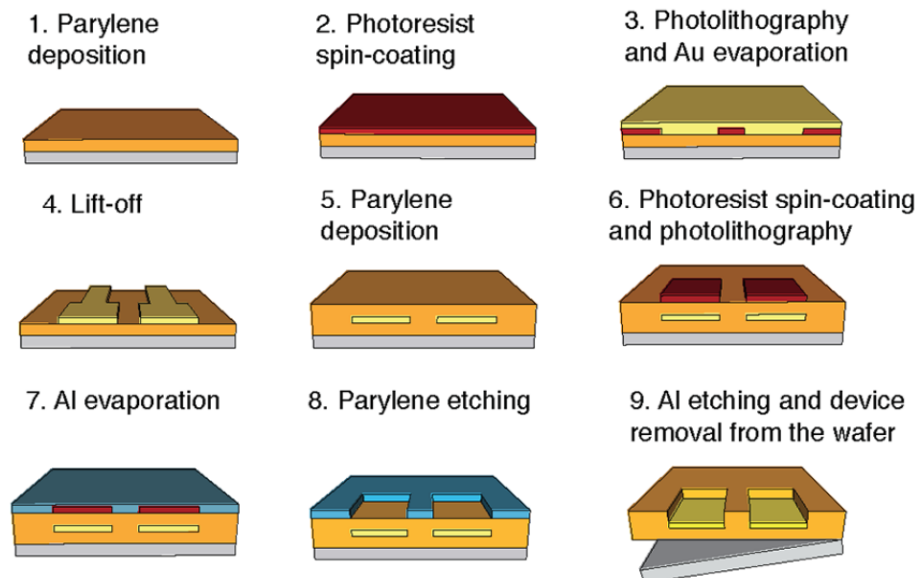


Figure 3. A typical fabrication process of microelectrodes [1]

Inkjet printing has emerged as an attractive drop-on-demand (DOD) patterning technique that directly jets various types of functional materials with micron resolution. The resolution and capability of inkjet printing is owed to advances in material dispensing technologies and accurate electronic alignment. This method creates mask-less patterns by sequentially depositing multiple layers of different materials without perturbing the previously deposited layers. The additive nature of this process makes it suitable to deposit a variety of materials counting dielectrics, conductors and active materials, on variety of substrates such organic and flexible substrates, plastic and papers, in addition to the conventional silicon and glass wafers. This allows for fast and cost-effective prototyping where, for instance, resistors and conductors can be manufactured simultaneously. A commercially available and well-known inkjet printer is provided by Fujifilm Dimatix. This material printer is capable of scaling designs up to 8×11 inch areas while maintaining a micron resolution in printing, in order of 20-50 μm , that is controlled by the spacing between the jetted drops (Figure 4B). The drops are formed and jetted out through 16 nozzles of 21 μm diameter and 254 μm spacing allowing for small drop volumes and therefore a generation of well controlled, micro-scaled patterns (Figure 4A) [3].

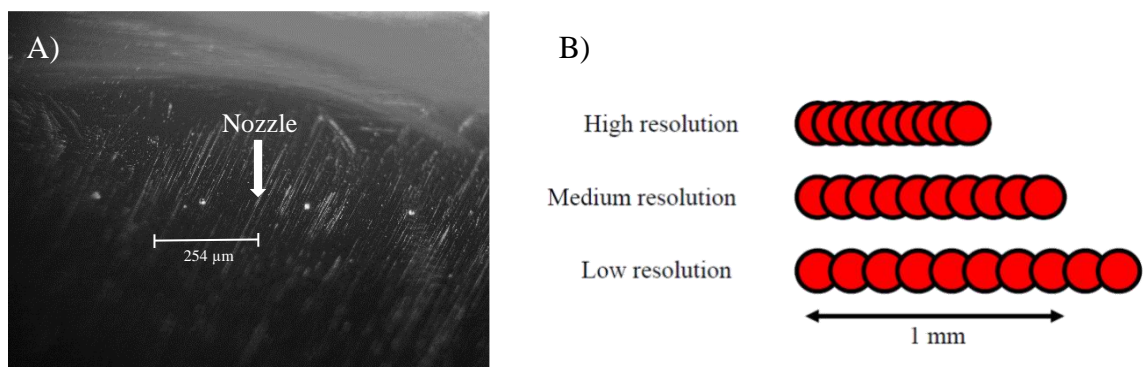


Figure 4. A) 1 pL nozzles in a 16-jet Dimatix Materials Cartridge. B) A line with a certain length can consist of more or less drops according to resolution (drop spacing)

2.7.1 Jetting Waveform

Producing an identical droplet essentially depends on the physical properties of each ink and the designed jetting waveforms. The latter is determined by voltage level, duration, and slew rate, and can be divided into multiple segments, each of which can be controlled independently (Figure 5). There is a direct relation between the voltage level and the volume of the pumping chamber. Figure 5 shows the stages of jetting for a basic waveform that consists of three segments. The standby position connects the previous waveform to the beginning of another, where the piezoelectric element is still deflected due to the previous pulse. Whenever the jetting pulse decreases (phase 1), the piezoelectric element relaxes, making the pumping chamber at its greatest capacity. At this phase, the ink flows into the chamber from the reservoir. The next phase of the pulse (phase 2) causes the chamber to be compressed where a pressure is generated for drop ejection. Here, the voltage level is back to the starting phase with its initial value and is ready for the next cycle. Although the slew rate has minimal influence on droplet formation, it determines how quick the volume of chamber changes. Generally, the pulse width, slew rate, amplitude, and frequency of jetting are important factors as they govern the size, shape, and speed of the droplets, thus controlling the overall printing quality.

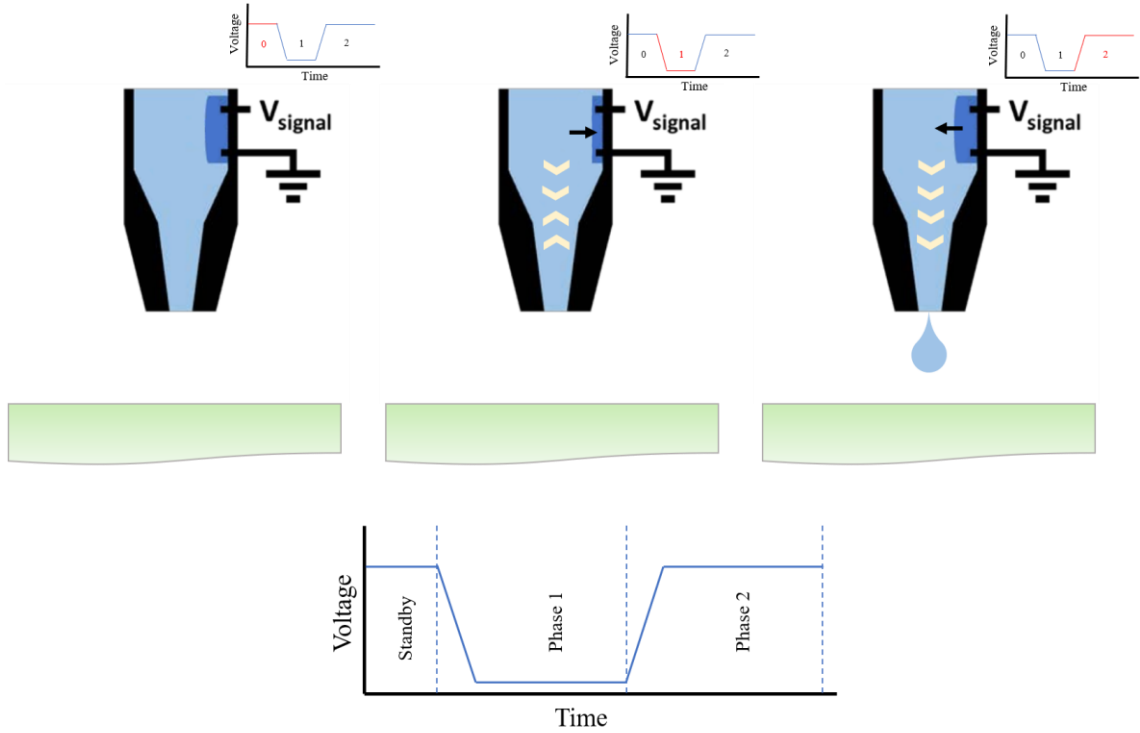


Figure 5. Schematic diagram of the print head with stages of jetting for a basic waveform

2.7.2 Ejectability Assessment

Ideal jetting waveforms depend mainly on the fluid characteristics. Thus, the waveform can be adjusted, including the number of segments, according to the fluid properties. One way to characterize fluid ejectability is to compute the Z number, which is a factor that is mainly affected by the physical properties of the fluid, including viscosity, density, and surface tension [69, 70]. This is given by the equation:

$$Z = \frac{\sqrt{\rho r \gamma}}{\mu} \quad (1)$$

Where μ is ink's viscosity, γ is the ink's surface tension, ρ is the ink's density and r is the diameter of the nozzle. As the value of Z decreases, the forces required to formulate and rupture the droplets increases [69, 71]. Usually, a range between 1 to 10 for the ink

indicates a good possibility to print via drop-on-demand method [70, 71]. A desirable and acceptable droplet formation is achieved when one primary droplet is ejected before making it to the substrate. Satellite droplets maybe generated directly after the main droplet depending on the primary droplet speed and the length of its thread tail. This effect is unfavorable as it can have a large impact on the printing quality. However, the jetting voltage and waveform play a role in minimizing this effect as explained in previous studies [72, 73].

CHAPTER 3

SPECIFIC AIMS

Aim #1: Fabrication and testing of biodegradable, flexible neural interface

Hypothesis A: We will test the hypothesis that the printed PEDOT:PSS electrodes can be fabricated onto a flexible substrate with micron resolution.

Hypothesis B: We will test the hypothesis that the PEDOT:PSS electrodes can be fabricated onto a biodegradable and biocompatible substrate.

Challenge: Integration of biodegradable, soft polymers with electrodes fabrication.

Approach: We will utilize a unique low temperature, high-resolution printing technology to realize our design.

Impact: Development of a unique biodegradable, inkjet-printed, and flexible interface that is able to record the neural activity without the damage resulting from device retraction or removal. In addition, printing technology enables quick and cost-effective tailoring of the device to patient or experimental needs.

Aim #2: Test the potential for the neural interface to record visual responses from the retina

Hypothesis A: We hypothesize that the neural interface can record visual responses from the retina, including spike recordings from retinal ganglion cells.

Hypothesis B: The neural interface is bioresorbable and biocompatible in vitro.

Challenge: Identify the proper parameters and conditions for recording the retinal activity in vitro.

Approach: We will extract the retina from the rat's eye and place the ganglion cells on the side of the flexible platform, then record activity via PEDOT:PSS electrodes.

Impact: This will serve as a feasibility study for the technology and offer insight into the parameters required to enhance the recording capabilities of the device.

CHAPTER 4

METHODOLOGY

Aim #1: Fabrication and testing of the biodegradable, flexible neural interface

In this aim, we embark on a new fabrication process that utilizes piezoelectric inkjet printing with micro level resolution to build a biodegradable, flexible neural interface with single-cell resolution.

Aim #1A: Testing the hypothesis that PEDOT:PSS printed electrodes can be fabricated onto a flexible substrate with micron resolution.

The processing was done via a commercially available material printer (DMP-2850, Fujifilm Dimatix, USA) fitted with a piezo-driven 16-nozzle printhead with a drop volume of 1 pL. This inkjet patterning unit requires the fluid's viscosity to be in the range of 10-12 cps in order to achieve optimum performance. As the commercially available materials have a relatively high viscosity, the addition of chemical solvents to modulate the viscosity may impact their electrochemical properties by reducing the thickness or adhesion to substrate leading to potentially increased impedance or reduced charge injection, both of which are essential for neural modulation and recording [74]. Therefore, the addition of these chemicals should be optimized to reach the maximum performance with the desired inkjettable viscosity. In this work, the all inkjet-printed array was patterned using Ag nanoparticles ink, then the electrodes were coated with multiple layers of PEDOT:PSS. Also, PEDOT:PSS coating was compared with graphene/PEDOT:PSS coating. Finally, the connection lines were insulated by dielectric ink.

Fabrication process: No modifications were applied to the Ag ink as its viscosity and surface tension are already compatible with the printer (736503, Sigma-Aldrich). For PEDOT:PSS coating, a dilution was obtained by adding some chemicals that have been shown to bring PEDOT: PSS to the ideal viscosity for inkjet printing. Water has constituted 50% of the PEDOT:PSS. Dimethyl sulfoxide (DMSO) (472301, Sigma-Aldrich) was also added with 5% to the total solution; a solvent that enhances the conductivity through screening effect [75]. Finally, the addition of a surfactant called Triton™ X-100 (Sigma-Aldrich) has modulated the surface tension of the mixture to meet the requirements of the printing process as well as to enhance the conductivity of the solution [76]. This additive will also improve the uniformity in the printed films and reduce coffee ring effect. Therefore the resulted dilution 1:1 PEDOT:PSS/H₂O + 5%DMSO + 1%Triton has brought PEDOT:PSS to the preferable fluid properties [77]. Although the coating was mainly achieved by the prepared PEDOT:PSS ink, a quick performance comparison was done to investigate how the coating materials significantly change the electrode performance. Therefore, graphene/PEDOT:PSS ink was used (900442, Sigma-Aldrich), and it consisted of PEDOT:PSS with a concentration 0.2 mg/mL and graphene with a concentration of 1 mg/mL, all dispersed in dimethylformamide (DMF). The printed coating films were annealed at 90°C for three hours in order to remove all residual liquid before testing them for stimulation and recording ability.

For the passivation layer, a polymer-based dielectric ink was formulated using 1-Hexanol as a solvent material with 17:1 w/w% ratio, between 1-Hexanol and the polymers. The recipe is composed of poly(4-vinylphenol) (PVPh) (436216, Sigma-Aldrich) and poly(melamine-co-formaldehyde) (PMF) (418560, Sigma-Aldrich) with 1:1

w/w% ratio [78]. This formulation has inkjettable properties that permitted a proper droplet formation (Figure 6) without satellite effect, in control of the waveform shown in table 4.2. The printed layer was then cured at 200°C for 1 hour on a hot plate to allow crosslinking. The fabrication process and the patterns designed for the arrays and are shown in figure 8 and figure 9, respectively. All printing parameters, including drop spacing which determines the thickness and resolution of the patterned films, were optimized to control the drop formation are summarized in table 4.2. We mainly fine-tuned the jetting waveforms according to each material's properties to get well-defined droplets that are stable and have no satellite effect. Before loading any ink in the cartridges, the viscosity, density, and surface tension of the solutions were measured and confirmed using rotational viscometer (FungiLab) and goniometer OCA 15EC (Dataphysics, Germany), via pendant drop analysis, respectively. Table 4.1 shows the physical properties of each ink, acquired from the previous step, and the calculated Z number for ejectability assessment. All Z values fall in the acceptable range (1-10), which allow the inks to be properly ejected. Figure 7 (A-D) shows the chemical structures of all polymers used in fabrication process of the PI-based array.

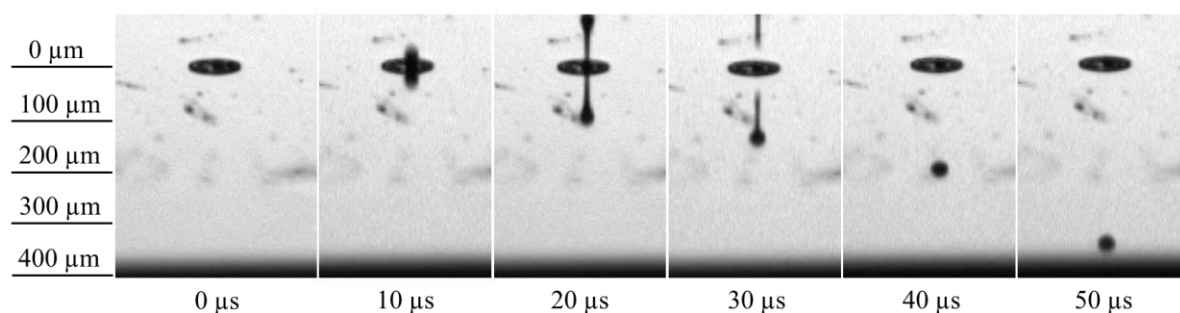


Figure 6. An example of droplet formation states taken via drop watcher camera for the PVPh ink

Table 4.1 Physical properties and printing indicator of the prepared inks at room temperature				
Material	Density (g/cm ³)	Viscosity (mPa.s)	Surface Tension (mN/m)	Z number
Ag nanoparticles	1.5	7	27	4.17
PVPh	0.956	13	29.3	1.87
PEDOT:PSS	1.024	12	9.44	1.19
Graphene/PEDOT:PSS	1.0012	8.08	39.57	3.57

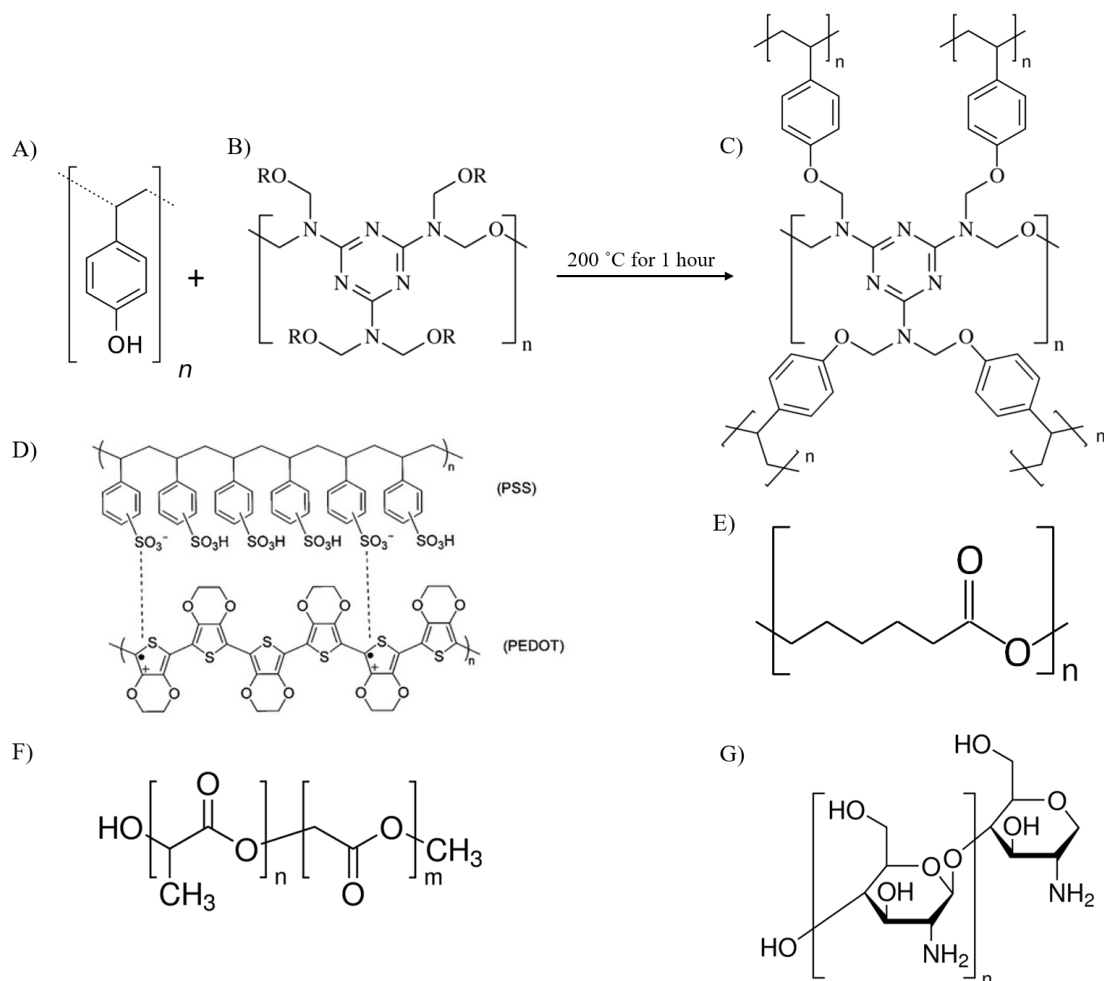


Figure 7. Chemical structures of A) PVPh, B) PMF, C) Crosslinked PVPh+PMF, D) PEDOT:PSS, E) PCL, F) PLGA, G) CS

Table 4.2 | Inkjet printing parameters for the deposition of the inks

Ink Type	Parameter	Value	Jetting Waveform
Ag nanoparticles	Print resolution	725.71 dpi	
	Drop separation	35 μm	
	Platen temperature	30 °C	
	Pulse width	8.576 μs	
	Jetting voltage	23 V	
	Jetting frequency	1 kHz	
	Substrate to printhead distance	0.3 mm	
PVPh dielectric	Print resolution	1693.33 dpi	
	Drop separation	15 μm	
	Platen temperature	50 °C	
	Pulse width	26.880 μs	
	Jetting voltage	24 V	
	Jetting frequency	2 kHz	
	Substrate to printhead distance	0.85 mm	
PEDOT:PSS and Graphene/PEDOT:PSS coatings	Print resolution	5080 dpi	
	Drop separation	5 μm	
	Platen temperature	30 °C	
	Pulse width	8.064 μs	
	Jetting voltage	23 V	
	Jetting frequency	1 kHz	
	Substrate to printhead distance	1 mm	

Electrochemical Characterization of the Microelectrodes: The electrochemical characterization was performed with a Potentiostat/Galvanostat/ZRA system (Gamry Instruments, USA) using a three-electrode cell. A glass beaker was filled with phosphate buffer saline (PBS), and platinum (Pt) was used as a counter electrode while Ag/AgCl was used as a reference electrode. As for the cyclic voltammetry (CV), the voltage was swept between -0.5 V to 0.5 V at a rate of 100 mV/s. The CV curves helped us in determining: (1) Water window; electrodes need to operate within a voltage limit to ensure the electrode potential remains under the range between hydrogen evolution potential (negative) and oxygen evolution potential (positive). (2) Charge storage capacity (CSC); an important parameter that represents the maximum charge that can be injected via reversible surface processes by an electrode. This number is obtained via integrating the area under the cathode or anode part of the CV curve within the water window:

$$CSC = \frac{1}{\nu A} \int_{E_c}^{E_a} |i| dE \quad (2)$$

with E presenting the negative and positive potential range vs. the reference electrode, i is the measured current, A is the electrode's surface area, and ν is the scan rate.

Using the same setup, the EIS was measured to determine whether the impedance falls within the acceptable range. This process is essential for both stimulating and recording electrodes. Recording the neural activity requires high spatial resolution with micro-scaled electrodes. Decreasing the size of the electrodes increases the impedance, thus producing noisy data. Typically, the levels of fluctuation noise that create recording problems come from electrodes with impedances of 5 M Ω or higher [79-81]. The same applies for stimulating neurons, as it requires large current densities and if the interface

impedance is too high, it will lead to higher levels of applied voltages that can potentially lead to irreversible redox reactions and puts a load on power requirements. The impedance values at 1 kHz were collected for comparison purposes since the characteristic frequency band of the action potentials is centered at 1 kHz. Measuring the electrode's impedance and CSC has facilitated in investigating the effect of depositing different number of PEDOT:PSS layers. The variation of the electrode's size was also investigated for verification.

Aim #1B: Testing the hypothesis that the printed PEDOT:PSS electrodes can be fabricated onto a biodegradable substrate.

Biodegradable flexible device backbone: Several biodegradable and biocompatible materials, that have the potential to serve as good substrates for our interface and match the specifications we indicated in design considerations, were tested. The first material is PCL (Figure 7E), which is easily processable in form of liquid solution to make thin and flexible films. The fact that PCL has a low melting temperature of 60°C limits the methods of post-treatment to be used with deposited films [52]. However, there are alternative ways to deal with the temperature limitation including intense light curing that will be mentioned in a later section. The second material used is PLGA (Figure 7F). It comes in an amorphous form and can be prepared easily like PCL. A blend of PCL and PLGA can be prepared to manipulate the degradation rate and mechanical properties of the interface to suit the type of application, since PLGA has relatively faster degradation rate. CS (Figure 7G) is another biocompatible material that usually used in coatings. CS is a polysaccharide with hydrophilic properties that can be used in coating surfaces to improve wettability and adhesion. CS film was prepared to act

as an intermediate layer that enhances wettability of the surface. It is important to mention that the surface roughness and morphology of all potential materials were compared with PI that was used in Aim #1A. PI is a known biocompatible but not biodegradable material. Therefore, it is widely used in bio-integrated devices due to its high biocompatibility and flexibility [60]. Thin, flexible films of each material, with $\sim 10\text{-}13\ \mu\text{m}$ thickness, were prepared to make the substrates conformal enough to accommodate the natural motions and anatomical shapes.

Fabrication process: The PCL solution was prepared with 20% w/v PCL of 9:1 chloroform to DMF. The PCL pellets, $M_w \sim 48,000\text{-}90,000\ \text{Da}$, (704105 Sigma-Aldrich) were added to chloroform and stirred at 50°C for 30 minutes. DMF was then added and mixed after visually ensuring that the PCL has completely dissolved. The PLGA (769827 Sigma-Aldrich) solution, with an inherent viscosity of $0.16\text{-}0.24\ \text{dL/g}$ and a 75:25 lactic:glycolic acid ratio was prepared as well with 4 wt.% in chloroform. A blend of PCL/PLGA (8:2) was also prepared for the degradation and mechanical experiments. Finally, CS (448877 Sigma-Aldrich) was prepared in 1 wt.% in 1% acetic acid. Both mixtures, PLGA and CS, were stirred for 24 hours on a stirrer prior using. Before the spinning process, glass slides were cleaned with isopropanol alcohol and rinsed with deionized water to serve as sacrificial substrates. A spin coater (WS-650MZ-23NPPB, Laurell Technologies Corporation) was used to prepare the films with 1000 rpm and 5 minutes of spinning duration. Upon inspection of PCL, PLGA, and CS films with scanning electron microscope (SEM), as will be shown in the results section, the PCL was chosen as our main biodegradable substrate for the rest of the report. The whole fabrication process for the PCL-based array is shown in figure 8(f-j). The fabrication process for the PCL-based array differs from that for PI-based array in two steps: the post-

treatment method of the Ag ink and PEDOT:PSS coating, and the dielectric material used. The latter consisted of heat-pressed PCL films that were accurately aligned around the electrodes.

Investigating the surface morphology of the substrates guides us on adjusting the printing properties to suit the nature of each material surface. For that reason, Surface roughness of the substrates was determined using a high resolution tapping atomic force microscope (AFM) (WITec, Germany). Optical microscope and SEM were utilized for surface topography investigation as well. The wettability of the substrates was measured by a standard goniometer (OCA 15EC, Dataphysics, Germany) with the sessile drop method and analysis software. The conformality and flexibility of the devices are also crucial properties to ensure mechanical matching between the tissue and implant. Having a device with mechanical properties that are similar to the neural tissue would reduce the immune response, tissue damage, and scar tissue. Therefore, the mechanical properties of the designed interface were determined, including the elastic moduli, using a mechanical testing machine (Instron, Norwood, MA) with a 10 N load cell at a strain rate of 50 mm/min. The results were compared with the elastic modulus of the neural tissue.

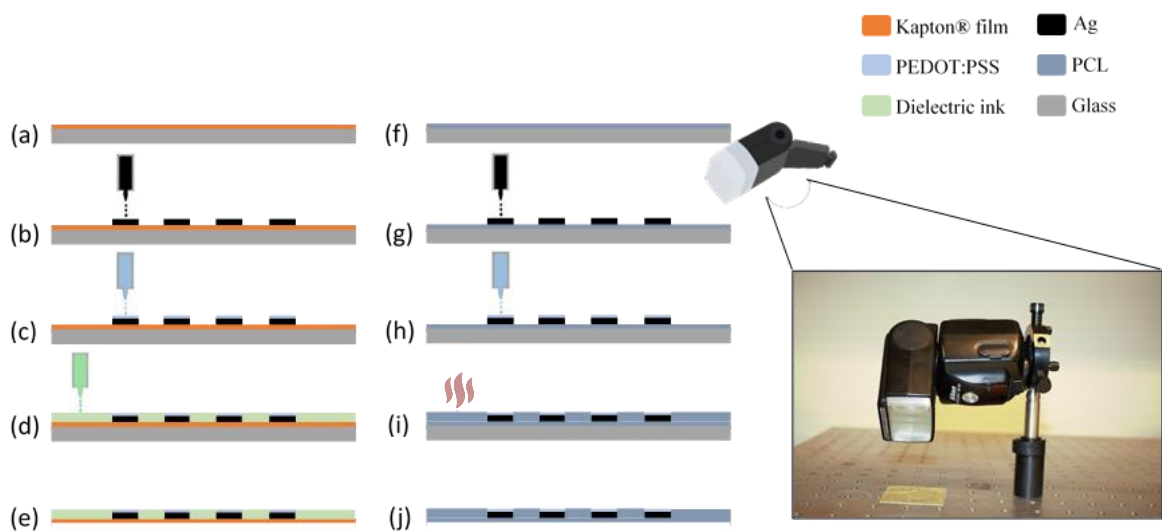


Figure 8. Fabrication process of Ag/PEDOT:PSS electrodes (a to e) on PI and (f to j) on PCL

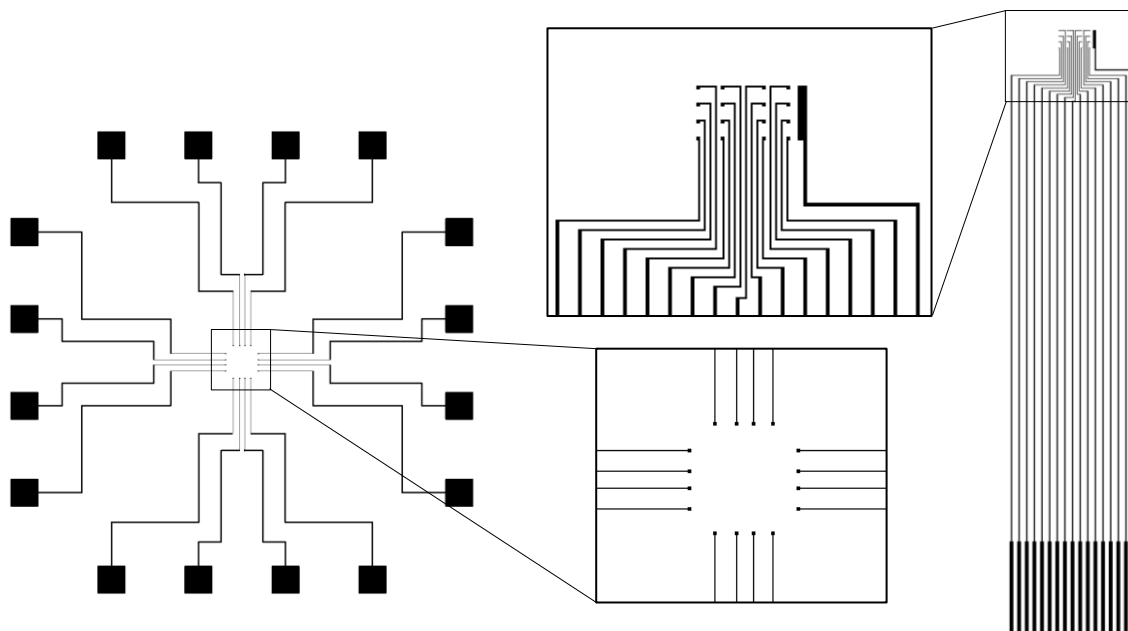


Figure 9. Top view of the electrode patterns

Light sintering setup and conditions: The commercially available AgNPs inks are usually stabilized by coating the NPs with stabilizing material/s. Once the NPs are thermally activated, the coating degrades, and the size of the particles slightly enlarge. Therefore, coalescence between the particles happens to create a conductive pattern (Figure 10). This thermally treatment process for the printed Ag patterns requires considerably high temperatures that could reach 250°C. Also, the annealing time can take hours. The high temperatures and long processing times eventually degrade the PCL substrate, thus, ruin the printed patterns. An alternative method is to sinter the nanoparticles using intense light pulses, or photonic curing [82]. Sending a high energy pulse for few milli-seconds instantly increases the temperature of the metallic ink, leaving the majority of the substrate relatively cool. In our setup, a camera flash-lamp (Nikon speedlight SB-28) was used to sinter the AgNPs and create the conductive paths for the electrodes (figure 8g) [83, 84]. The substrate was placed 1 cm away from the light source,

and an aluminum reflector was used to uniformly distribute the light on the overall pattern. The substrate was exposed to multiple consecutive pulses with a pulse width of 1 ms and off period of 2 seconds (Figure 11). A certain number of pulses creates a conductive pattern, however, exceeding this number could lead to defects in the pattern. Therefore, the required number of pulses and sintering conditions were investigated. A four-point probe system (Ossila, UK) was used to study the effect of each pulse on the pattern, where the resistance of the printed Ag was measured directly after each pulse. This technique, which is also known as Kelvin technique, is based on using four electrical probes that are equally spaced in line (Figure 12). A current is applied by the outer two probes, while the two inner probes are used to measure the voltage. The sheet resistance of the films is then calculated via the I-V curve according to the equation:

$$R_{sheet} = \frac{\pi}{\ln(2)} \frac{\Delta V}{I} \quad (3)$$

Eliminating the effect of wire resistances and surface contact from the measurement is a primary advantage of using such system for electrical characterization.

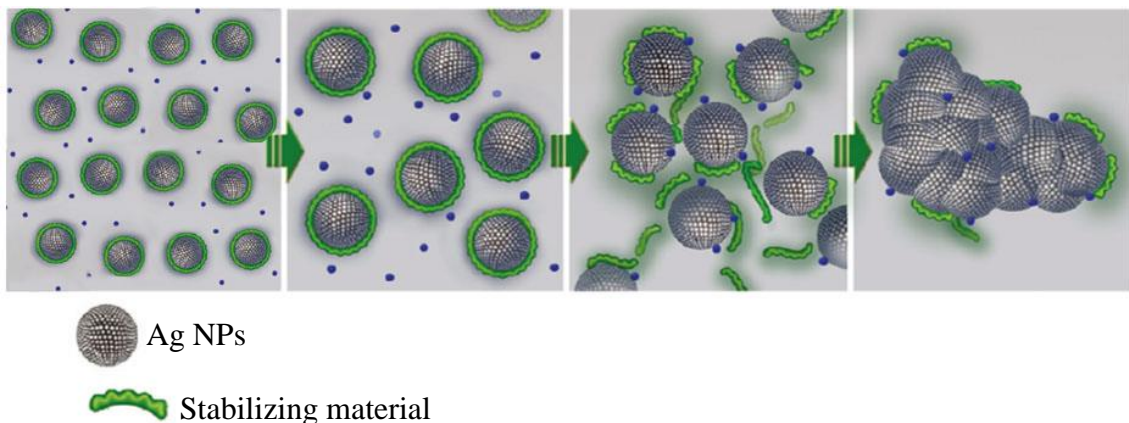


Figure 10. Schematic illustration of NPs' sintering process. Adapted from [85].

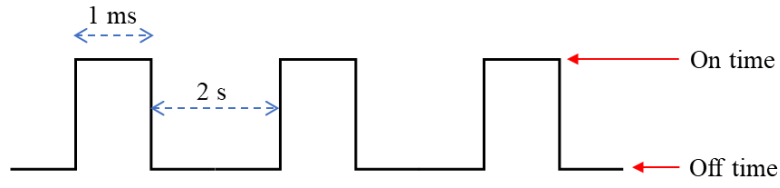


Figure 11. Schematic of consecutive light pulses with 1 ms pulse width

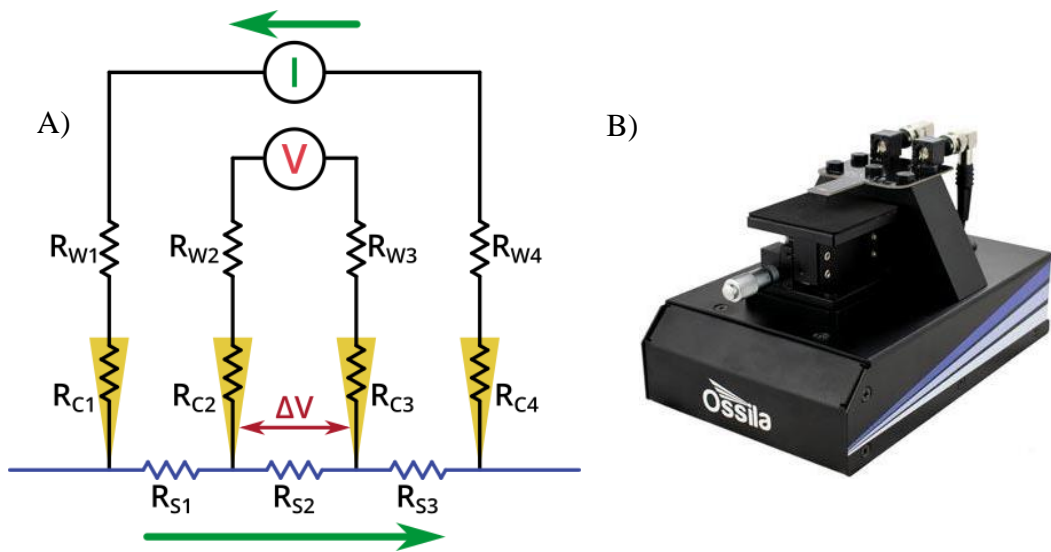


Figure 12. A) Schematic diagram of a four-point probe circuit, B) Four-point probe system (Ossila)

Aim #2: Test the potential for the neural interface to record visual responses from the retina

In this aim, we determined the efficacy of the interface by recording spontaneous neural activity from the retina with high signal to noise ratio.

Aim #2A: Testing the hypothesis that the neural interface can record visual responses from the retina, including spike recordings from retinal ganglion cells.

Experimental Design

Retinas were dissected from carbon dioxide euthanized eyes that were obtained from Sprague/Dawley rats. They were removed using methods described in previous work [86]. Sodium bicarbonate was used to buffer AMES solution, then it was oxygenated to bring the medium pH to 7.4. Retinas were dissected into 4×4 mm retinal segments, and were kept in the AMES solution at 37°C. The retina segment was transferred onto the prepared device which was connected to the ME2100 system (Multi Channel Systems, Germany) as shown in figure 13. A chamber over the active area of the device was attached to add media to the cells. The extracted retina was placed with the ganglion cells facing the electrodes. To enhance tissue adhesion and increase the wettability of the surface, the array was ozone cleaned for 45 minutes exactly before placing the retina. The system was equipped with a perfusion system to supply the tissue with fresh solution so that the retina is maintained for the longest time. Offline sorter software (Plexon Inc, Dallas, TX) was used to analyze the data and detect a single unit activity. A threshold of 4 times standard deviation of the noise was set for the spike activity [87]. The recorded spikes passing threshold were then fitted to preloaded templates matching features of neuronal spike activity. Data was collected simultaneously from all designed electrodes.

For light responses experiment, A 500 ms squared pulse with an intensity of 5 V was generated via ARDUINO to activate the LED circuit, which consisted of a white LED connected in series to a 61.9 Ω resistor. This corresponds to a high photopic light stimulus comparable to broad daylight that effectively activates cone photoreceptors. Single pulses every 2 s were used to perform optical stimulation of the retina.

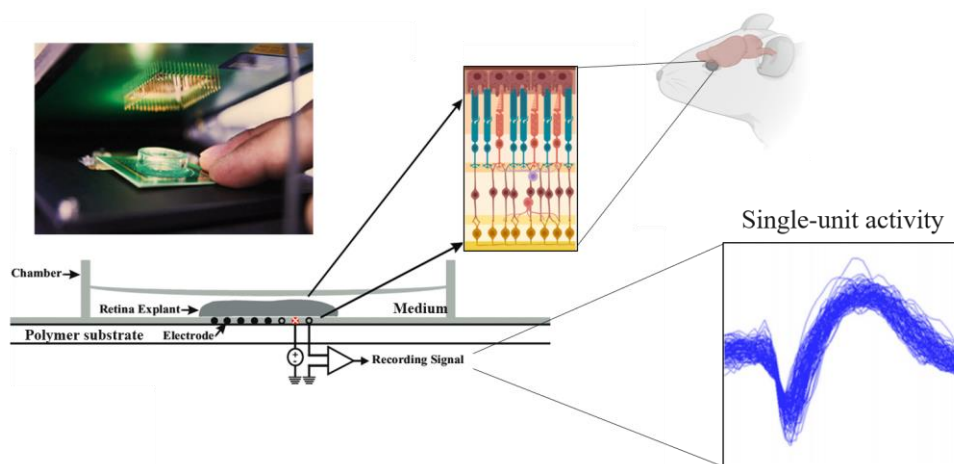


Figure 13. The general recording setup for the electrophysiological activity of the retina

Aim #2B: We hypothesize that the neural interface is bioresorbable and biocompatible in vitro.

The following aim details our efforts to test and confirm the biocompatibility and biodegradability of the neural interface.

Experimental Design

Meeting some strict biocompatibility standards is an important issue for a successful device implantation. Thus, PC12 cells were used to verify biocompatibility on the PI- and PCL-based arrays. PC12 cell line is originally derived from the adrenal medulla; specifically, the neural crest cells. The cells were cultured in Dulbecco's

Modified Eagle's Medium (DMEM) (D5796, Sigma-Aldrich) supplemented with 10% fetal bovine serum (FBS) and 1% Pen/Strep (antibiotics) and maintained in a humidified incubator at 37 °C with 5% CO₂. At 80% cell confluency, the cells were dissociated with trypsin, centrifuged and resuspended in fresh medium for seeding. The whole cell culture process was performed in Laminar Flow Hood (LabGard, Class II, Type A2 Biosafety Cabinet, USA) to prevent contamination.

For cell culture experiments, PI-based arrays were sterilized by autoclaving with a maximum ramping temperature of 132 °C for 30 minutes. On the other hand, PCL-based arrays were fixed on a petri dish with PDMS as an adhesive, sterilized by UV light irradiation (type C) with an intensity of 100 μW/cm² for 6 hours, then equilibrated in sterile 1X-PBS for 24 hours. Each array was immersed in medium inside a separate petri dish for few minutes before cell seeding. Cells were distributed on the substrates by dripping using a glass pipette. The adhesion behavior and morphology of the cells were monitored every 24 hours using a phase-contrast inverted microscope. Tissue culture plastic (TCP) was used as a positive control.

The viability of the cells was assessed by Trypan Blue (TB) Exclusion Assay. Generally, TB can only penetrate dead cells with compromised cell membranes; staining them with dark-blue color. The percentage of living cells was determined by counting the live and dead cells via image analyses using image software package (ImageJ). The results from PI and PCL substrates, with arrays printed on them, were compared to the ones without arrays serving as control. This control will ensure nothing in the processing could cause cytotoxicity. In addition, the results taken from PI and PCL substrates were compared to the TCP control values. This test was repeated 2 times (N=2).

Owing to its high molecular weight, ~ 48,000-90,000 Da, PCL has a slow degradation rate that could reach 2-3 years. Due to the long degradation time, an accelerated dissolution of the PCL-based array was induced by immersion the complete array (22×22×0.015 mm) in buffer solution (pH 13) at 37 °C. For comparison purposes, a blend of PCL/PLGA (8:2) was also prepared to accelerate the degradation process. This quick study was conducted to observe the degradation behavior of the interface.

CHAPTER 5

RESULTS

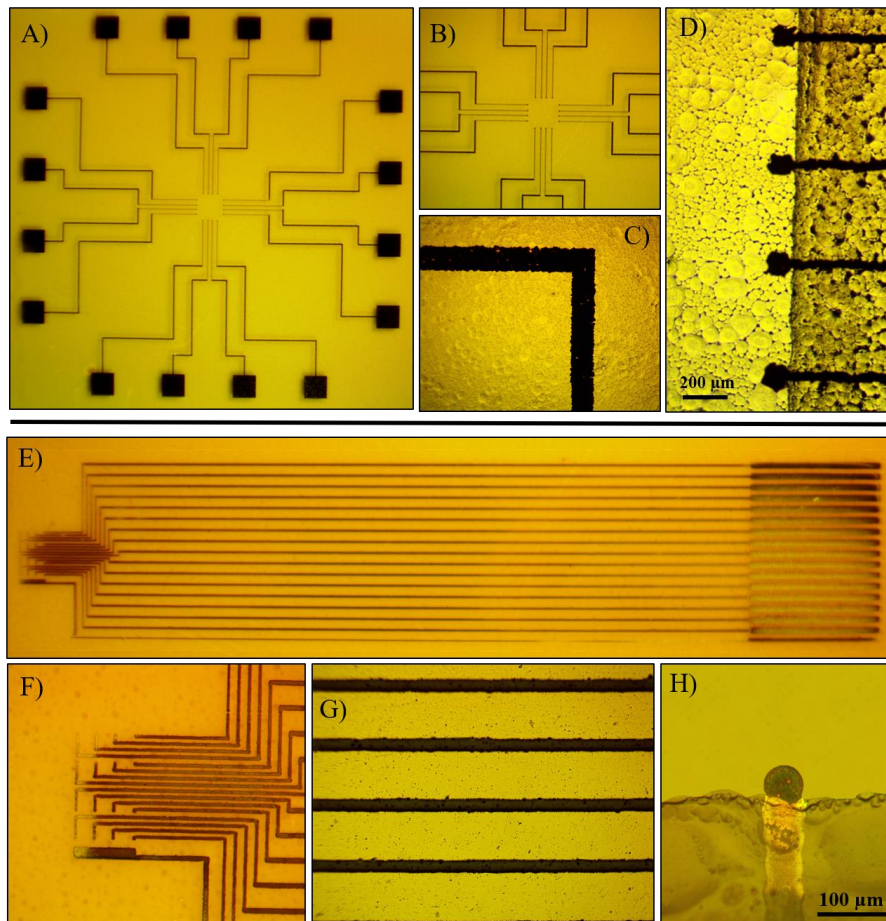


Figure 14. A) A 16-electrode biodegradable neural interface printed on PCL. B, C) Closeup of Ag-nanoparticles electrode leads printed with 100 μm line width on PCL. D) Closeup of recording sites where Ag-nanoparticles leads terminate with PEDOT:PSS electrodes of 70 μm . The leads are passivated with PCL. E) A 16-electrode neural interface printed on PI. F, G) Closeup of Ag-nanoparticles electrode leads printed with 50 μm line width on PCL. H) Closeup of recording electrode where Ag-nanoparticles lead terminate with PEDOT:PSS-coated electrode of 50 μm . The leads are passivated with PVPh.

In this work, two different array-patterns were designed and inkjet-printed on two types of substrates: PI and PCL. The pattern printed on PCL was designed to be connected to MEA2100 system, while the pattern printed on PI was designed to be connected to

ME2100 via a zifboard. Both arrays have 16 electrodes. The diameter of the electrodes on PI was 40-50 μm , while the diameter of the electrodes on PCL was 70-100 μm . Figure 14. (d, h) shows single electrodes with the printed coating, along with PCL (d) and PVPh (h) as insulation layers. Raman spectroscopy is conducted to ensure that chemical properties of the diluted PEDOT:PSS are maintained after the additives and thermal treatment. The Raman spectrum shown in figure 15 exhibited the main bands of the PEDOT:PSS ink. A strong vibrational band, that is related to the aromatic $C = C$ symmetric stretching is centered at 1438 cm^{-1} . Other two significant bands which correspond to $C_{\alpha} - C_{\alpha}$ inter-ring stretching and $C_{\alpha} - C_{\alpha}$ anti-symmetric stretching are found at 1253, 1533 cm^{-1} , respectively. Although PEDOT:PSS ink was diluted and treated at 90 $^{\circ}\text{C}$ for three hours after printing, the Raman spectrum showed similar features with no significant changes, when compared to previous studies [88, 89]. The lab-prepared

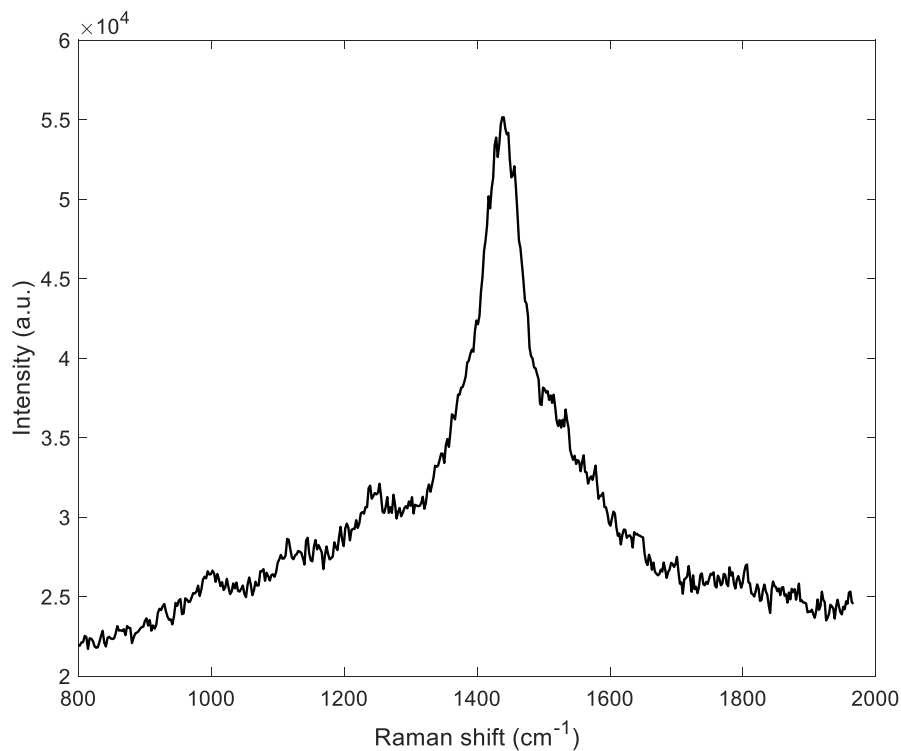


Figure 15. Raman spectrum of thermally treated PEDOT:PSS films at 90 $^{\circ}\text{C}$ for 3 hours

PEDOT:PSS dilution also showed the expected jetting behavior, printing quality, and electrochemical performance. In addition, all the inks used in the printing process noticeably exhibited a uniform distribution of material content throughout the printed films except for the PVPh ink. In other words, the evaporation nature of the solvents in the PVPh ink usually causes what is called, coffee ring effect. However, annealing the PVPh films at 200 °C reduced this effect, to some extent, and provided adequate insulation.

5.1 Surface Characterization

As mentioned in Chapter 4, different materials were chosen as potential substrates for our device. The surface morphology and roughness of the substrate are very important properties that must be considered before starting the printing process since they determine the contact angle of each jetted droplet. In figure 16, SEM images show the surface topography of spin coated CS, PCL,

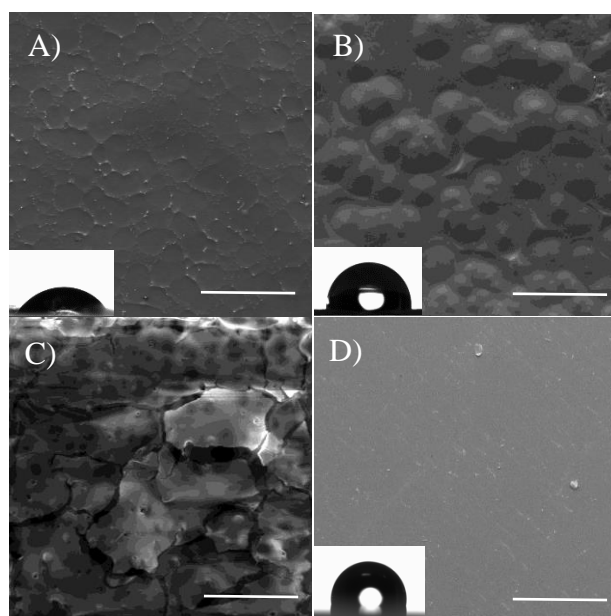


Figure 16. SEM images showing the surface morphology for A) CS, B) PCL, C) PLGA, and D) PI. All scale bars indicate 200 μm

PLGA and commercially available PI film. The CS displayed a quite smooth surface with some small ripples (Figure 16A) while PCL showed island-like raises (Figure 16B). These microstructures make the surface rougher, thus more hydrophobic. However, they have complicated the printing process and effected the shape of the electrodes. This is the

reason for making the diameter of the electrodes slightly larger than those printed on PI (~70 μm). On the other hand, PI featured relatively smooth and highly hydrophobic surface. PLGA showed multiple cracks and pores which made it not suitable for printing (Figure 16C). Some manipulations can be applied on the PLGA formulation and treatment conditions whether by changing the polymer to solvent ratio, or the ratio between poly lactic acid (PLA) and poly glycolic acid (PGA). The contact angle ' θ ' values characterized the degree of wettability of each film, which were 67°, 91°, 104° for CS, PCL, and PI respectively. Typical standard deviations are of the order of 0.6. PCL and PI substrates showed the optimal printing conditions including excellent ink adhesion and post-deposition droplet formation.

To further investigate the dependency of the printing quality on the surface roughness, plasma etcher was utilized. Multiple Ag lines were printed on several PI films with a varied etching time. The PI films were plasma etched with power of 100 W and different plasma times of 10 minutes, 20 minutes, and 30 minutes. The AFM images shown in figure 17 demonstrate the difference in surface roughness between the plasma-treated substrates. The maximum roughness of the non-treated, 10 minutes-, 20 minutes-, and 30 minutes-plasma treated films is 7 nm, 13.17 nm, 27.23 nm, and 50.17 nm, respectively. As

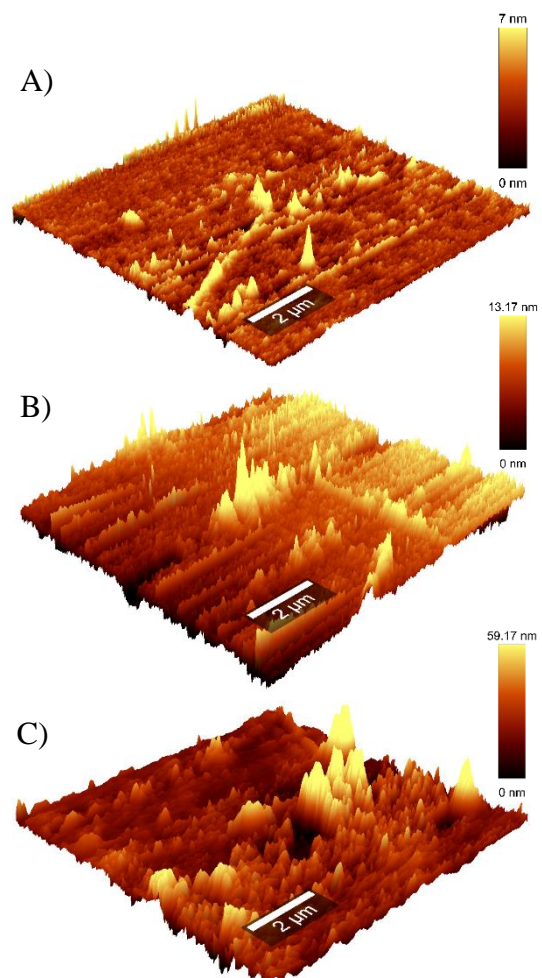


Figure 17. AFM images of PI plasma-treated substrates: A) no treatment, B) 10 minutes etching, and C) 30 minutes etching

noticed, the roughness of the surface increases with etching duration. Table 5.1 represents the average of contact angle and line width for the plasma treated PI films. The contact angle dramatically decreased from $\sim 104^\circ$ to $\sim 13^\circ$ after 10 minutes of etching, making the surface hydrophilic. Also, the printed lines showed a noticeable variation in the width compared to the actual widths. Etching the samples up to 10 minutes gave us patterns that are clean and very close to the actual widths. However, when the etching duration increased above 10 minutes, the wettability noticeably increased beyond our need, which lead to spread of the ink and therefore wider lines. Therefore, we concluded that plasma etching helps in optimizing ink-to-substrate wettability to a certain extent.

Table 5.1 Average of contact angles and widths of lines inkjet printed on plasma treated PI films				
	Non-treated	10 min	20 min	30 min
Contact Angle (°)	104.58	12.98	5.83	5.30
Setting Width (μm)	Actual Width (μm)			
30	33.5	33.26	36.75	40.81
40	44.06	41.56	44.69	52.65
50	54.13	53.66	56.28	58.35
60	64.58	57.14	63.73	64.7
70	70.05	75.44	70.1	74.24
80	73.97	76.97	75.29	85.91

5.2 Mechanical Testing

The mechanical testing was conducted for 6 samples of both PI and PCL substrates, having similar thickness of 13 μm. All samples had same dimensions and thicknesses for accurate comparison. It is noticed that the substrates exhibited high flexibility and conformality, which allows the interface to take the shape of the brain surface (Figure 18C). This mechanical characteristic is extremely important in reducing the immune responses. The PCL and PI samples showed a Young's modulus of 24 MPa

and 1.37 GPa, with a maximum tensile stress of 2.5 MPa and 47 MPa respectively (Figure 19A). However, PCL substrates showed a maximum elongation of 4.05 mm, which is higher when compared to a value of 0.16 mm for PI substrates. It worth mentioning that the modulus value of PCL is high compared to brain tissues (in kPa), but it is relatively very low compared to PI. Adding the insulation layer on the PI substrates changed its mechanical properties in which the Young's modulus increased up to 4.9 GPa (Figure 19B). This is due to the crosslinked molecules inside the PVPh, which elevates the overall substrate's maximum tensile stress up to 60 MPa and reduces its maximum elongation down to 0.12 mm. The blended substrates (PCL/PLGA), that were used to tailor the degradation rate, showed higher modulus of 187 MPa compared to pure PCL substrates (Figure 19C). In addition, blending with PLGA tremendously decreased the maximum elongation of the substrates to 30 μ m, and increased the maximum tensile stress to 3.5 MPa.

A brief simulation study was designed to investigate the actual mechanical behavior of the implanted interface *in vivo*. The data obtained from the previous step were used to design a mechanical model that simulates *in vivo* implantation and study the mechanical responses of the biodegradable interface when different surrounding forces are applied, such as shear forces from cerebrospinal fluid (CSF), outside surroundings, and repeatable forces from skull. Using ANSYS software, one type of forces was applied for simplicity. A uniaxial tensile force was applied from the circuit connection side while fixing the main part of the interface to be in contact with the brain tissue. As shown in figure 18, the fracture happens first at the corners of the device, where the main part is connected to the rest of the circuit, due to the concentration of stress there. However, as the simulation shows, the device can withstand forces with minimum fracture and with a

maximum elongation of 5 mm. However, such elongation may cause defects in the printed patterns, which consequently increase the resistance or lead to complete disconnection. It is important to highlight that the simulation was not conducted under fully mechanically challenged conditions, whereby the surrounding mechanical forces exerted by the skull and brain tissue are not considered. Therefore, the effect of these forces and even the micromotions on the interface's performance must be integrated in the model.

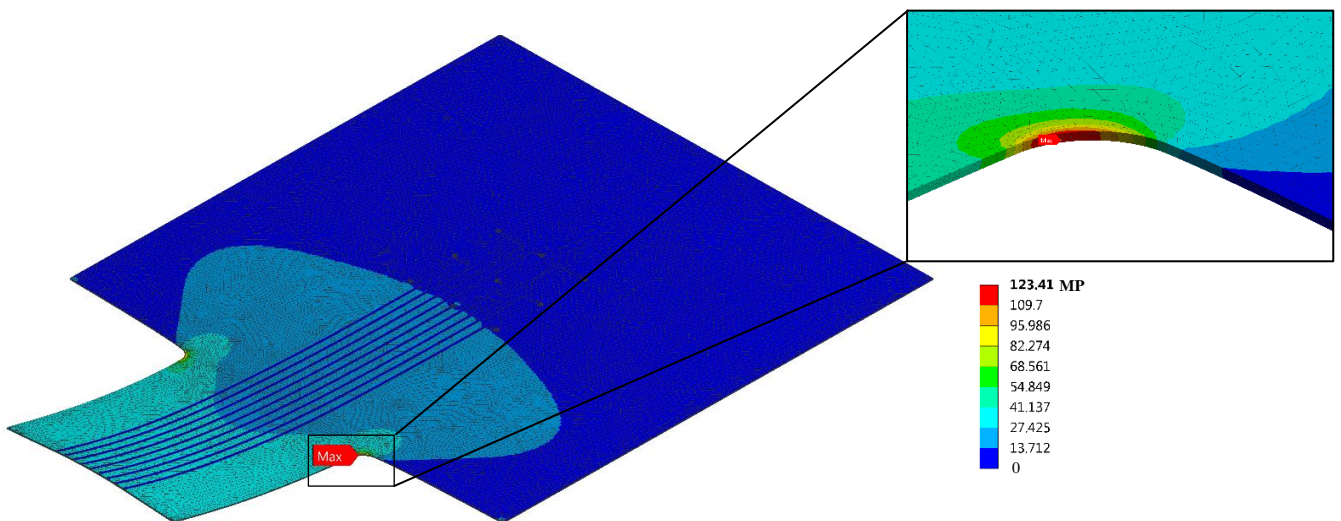


Figure 18. The distribution of stress in the PCL microelectrode array with a thickness of 13 μm at the fracture critical state

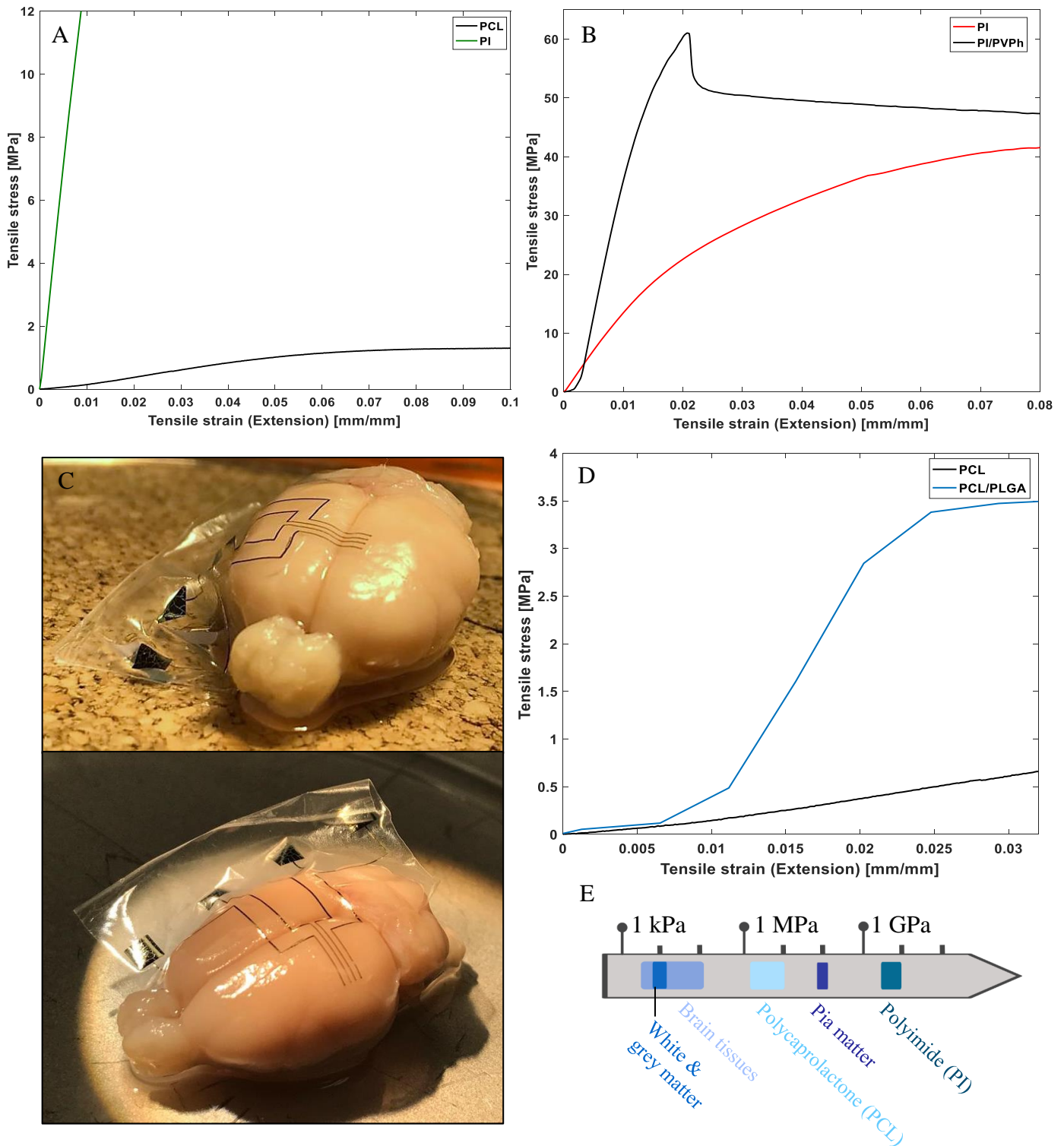


Figure 19. Stress-strain analysis of A) PCL vs. PI, B) PI vs. PI/PVPh, and D) PCL vs. PCL/PLGA. C) Microphotographic photos for soft conformal PCL-based array showing 4 electrodes lying on the surface of rat brain E) Schematic scaling that shows the mechanical properties of the brain tissue and utilized polymers

5.3 Electrochemical Characterization

In this work, PEDOT:PSS was coated on the surface of the Ag electrode by inkjet printing. Figures 20 shows the impedance spectra and CV responses of the microelectrodes with different number of coating layers and surface area. For layers variation, the diameter of the electrode was kept constant for all trials ($d=50\ \mu\text{m}$). The number of coating layers was 1, 3, 5, 7, and 10 layers. Figures 20 and 21A show the mean impedance of the printed electrodes, where the impedance decreases as the number of PEDOT:PSS layers increases. The combination of Ag and 10 layers of PEDOT:PSS exhibited the lowest impedance, where at 1 kHz, the average impedance value has reached $\sim 200\ \Omega$. Furthermore, the CSC value, that is obtained by calculating the area under the CV curve, is at its maximum with the 10-layers electrode. Figure 21B and 21C show an increase in the CSC values as the number of PEDOT:PSS layers increased. The detailed CSC average values for the 1-, 3-, 5-, 7-, and 10-layers electrodes are 1.08, 0.776, 1.18, 1.54, and $2.88\ \text{C}/\text{cm}^2$, respectively ($n = 6$ for each). Figures 22C and 22D show the EIS and CV responses for $50\ \mu\text{m}$ electrodes coated by single layers of PEDOT:PSS versus graphene/PEDOT:PSS. The electrochemical performance for the electrode coated by graphene/PEDOT:PSS was significantly enhanced compared to the one coated by PEDOT:PSS alone. In other words, a single layer of graphene/PEDOT:PSS exhibited a high electrochemical performance that is equivalent to 7 layers of PEDOT:PSS alone. As the thickness of the electrodes increased, the overall effective surface area increases. Using PEDOT:PSS, as a conductive polymer, adds electrochemical means to the electrode by increasing the charge delivery capacity and minimizing the impedance effect. We can conclude that using both the topographical and chemical approaches with

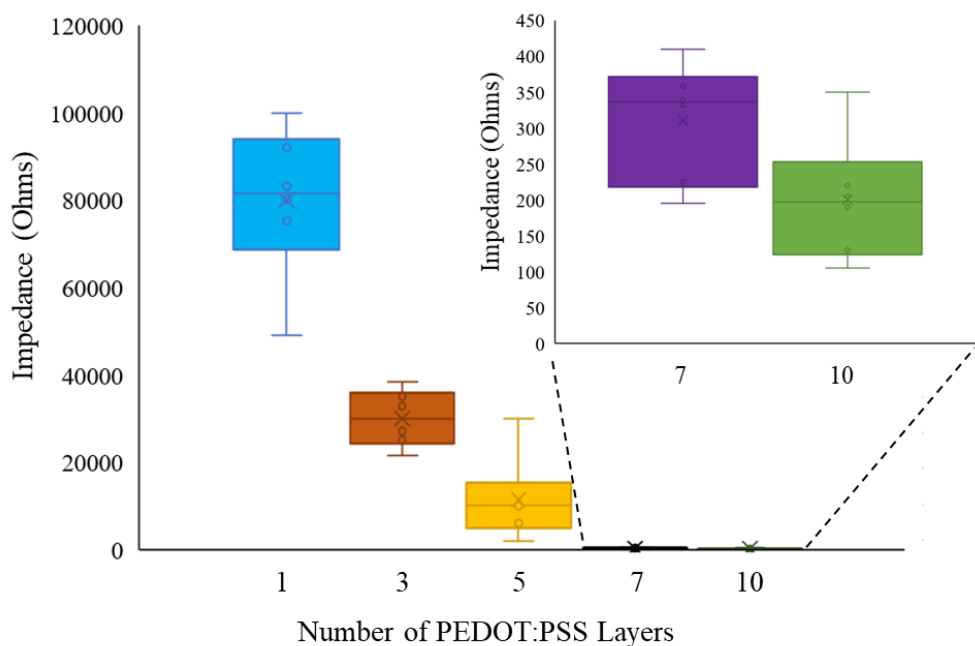


Figure 20. Impedance magnitude at 1 kHz on 50 μm electrodes

an increased number of layers leads to a significant enhancement of the electrode performance. Usually, increasing the thickness of the electrodes with a conductive, biocompatible polymer like PEDOT:PSS is not easily achieved by conventional fabrication techniques. The ability of the inkjet printer to deposit thin layers each time without affecting the underlying films, has increased the chance to enhance the performance of the electrodes. It is also observed that the impedance of the electrodes has decreased when the printed coating films were thermally annealed at 150°C for 30 minutes, as the presence of residual water normally affects the electrochemical interaction. Moreover, varying the surface area of the electrode directly affects the electrochemical performance. The diameter of the electrodes ranged between 30 to 100 μm . Although the impedance variation falls within one order of magnitude, the larger the area of the electrode, the lower the impedance (Figure 21D). Same applies for the CV responses, where the CSC values increased with the area (Figure 21E and 21F). The

detailed CSC average values for the 30 μm , 65 μm , 75 μm , and 100 μm electrodes are 1.01, 1.14, 2.98, and 10.87 C/cm^2 , respectively ($n = 3$ for each). In summary, the results explain the direct effect of the effective surface area of a flat electrode on both impedance and charge transfer.

Finally, an electrochemical performance comparison between the electrodes on PI substrate versus PCL substrate was conducted. As the post-treatment process of the printed patterns differs between PI and PCL, the adhesion, conductivity and stability of the electrodes change. Figures 22A and 22B show the impedance and CV responses of electrodes on PI versus PCL, having the same surface area. The average impedance value for the electrodes printed on PCL is 18.08 $\text{k}\Omega$ at 1 KHz . As noticed, the electrodes on PI exhibit lower impedance and higher CSC. However, the electrochemical performance of the electrodes printed on PCL still falls in the acceptable range ($< 5 \text{ M}\Omega$).

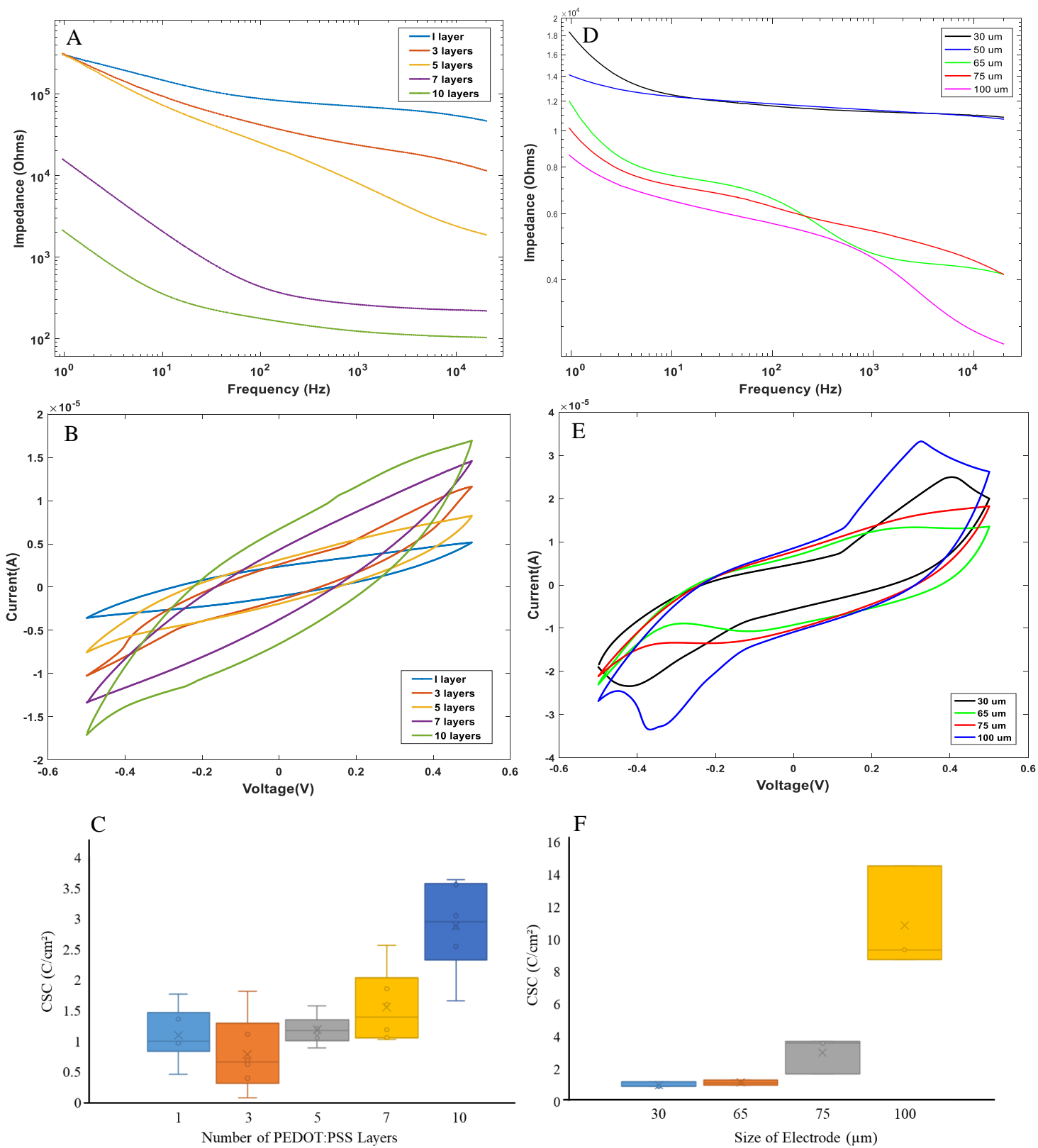


Figure 21. A) EIS shows impact of PEDOT:PSS multiple layer printing on 50 μm electrode impedance (lower impedance results in lower recording noise). D) EIS shows impact of PEDOT:PSS electrode diameter on electrode impedance. B, E, C, F) Figures show the impact of number of PEDOT:PSS layers and electrode diameter on CSC, data essential to evaluate the amount of charge delivered by electrodes.

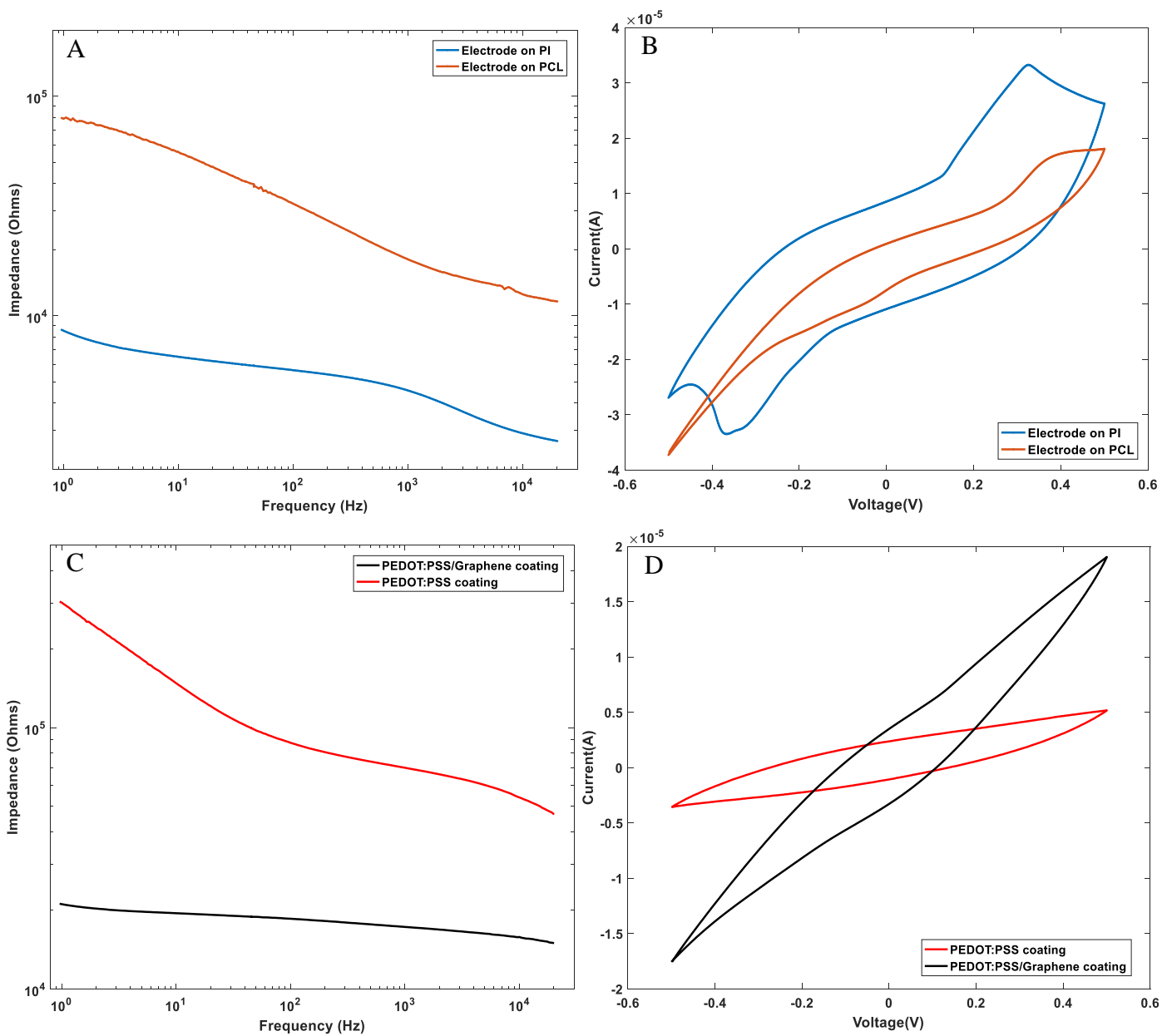


Figure 22. A) EIS shows the difference in impedance between 50 μm electrodes printed on PI vs. PCL. B) CV responses for 50 μm electrodes printed on PI vs. PCL. C) EIS shows the impact of coating material on 50 μm electrode impedance (lower impedance with graphene/PEDOT:PSS coating). D) CV shows the impact of coating material on 50 μm electrode CSC (higher CSC with graphene/PEDOT:PSS coating).

5.4 Ag Ink Sintering

As the photonic sintering technique was used for the biodegradable PCL substrate, the resistance of the photonic sintered silver was measured and compared with the thermally sintered samples. Although PI can withstand very high temperatures and can be used for thermal sintering, light sintering on PI substrate was conducted as well for comparison. As expected, the size of the NPs changes whenever thermal or light sintering is applied. The size of the nanoparticles before sintering is ≤ 10 nm. After thermal and photonic sintering, the size of the particles has enlarged to ~ 50 nm. The SEM images of three printed samples before and after sintering are shown in figure 25. It is also confirmed, from the SEM images, that during the sintering process, the Ag patterns become electrically-conductive whenever coalescence between the particles happens. Figures 25B and 25C show the difference between thermal and light sintering according to the degree of coalescence. The coalescence of the nanoparticles is tighter in the samples that were thermally-treated compared to those exposed to pulses of flash light. Therefore, the conductivity of the thermally-treated Ag patterns is the highest. Table 5.2 and figure 24 demonstrate the sheet resistance of the inkjet-printed Ag with respect of flashing numbers.

	Sheet Resistance (Ω/sq)
Single pulse	$1.136 \pm 7.5 \times 10^{-4}$
Two consecutive pulses	$0.789 \pm 4.2 \times 10^{-4}$
Three consecutive pulses	$0.861 \pm 2.1 \times 10^{-4}$
Thermally sintered at 250°C	$0.034 \pm 2.3 \times 10^{-4}$

Both patterns that were printed on PI and PCL became conductive after the first light pulse. The pattern on PI substrate has lower resistance than that on PCL. This is explained by the surface and material nature of each substrate. In other words, PI substrate

is more mechanically and thermally stable than PCL substrate, therefore fewer surface defects were observed on it (Figure 23B). On the other hand, The Ag pattern on PCL substrate experienced an increase in surface roughness and defects, which eventually lowered the thickness uniformity, thus higher sheet resistance (Figure 23A).

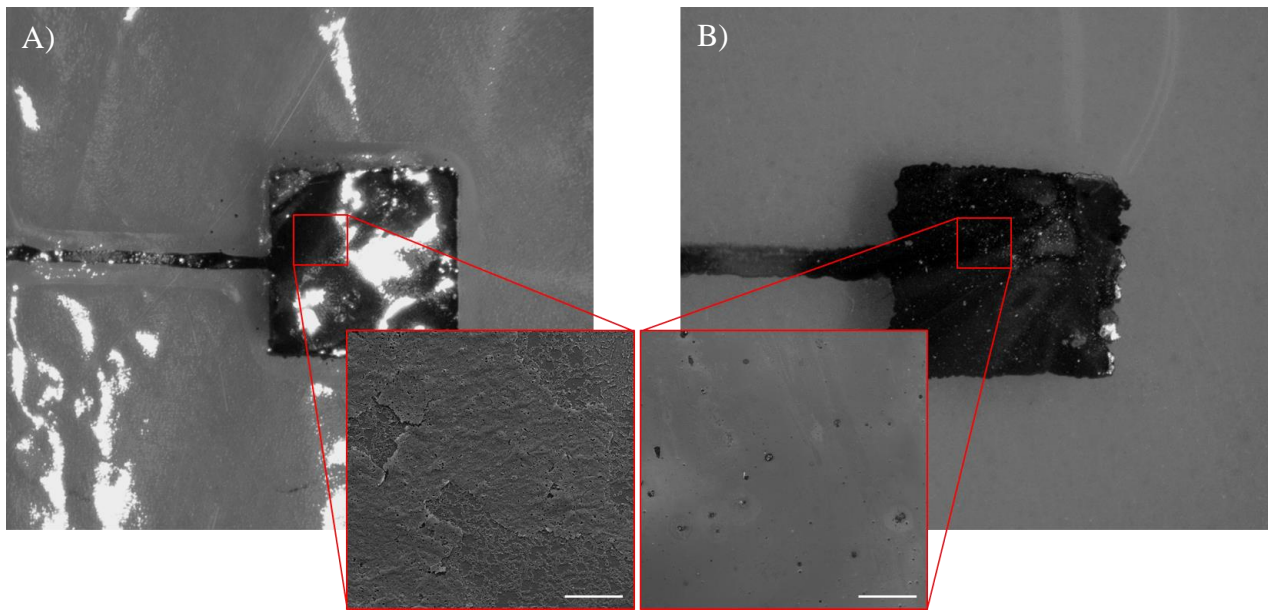


Figure 23. Microscopic and SEM images of typical Ag patterns on A) PCL and B) PI after flashing two times. SEM images show the morphology changes on the surface of the electrodes after treatment. Scale bars indicate 200 μm

As seen from figure 24, the resistance has clearly reduced after the second light pulse for the pattern printed on the PCL substrate, while the resistance was almost constant throughout the pulses for the pattern printed on the PI substrate. The resistance has increased after the third pulse, due to additional defects and cracks generation which caused interfacial delamination between the Ag film and the PCL substrate. Hence, two consecutive pulses with 1 msec duration were adequate to achieve a resistance of $0.789 \pm 4.2 \times 10^{-4}$ without degradation of the PCL substrate. This result is comparable to what has been reported by similar studies [83, 90].

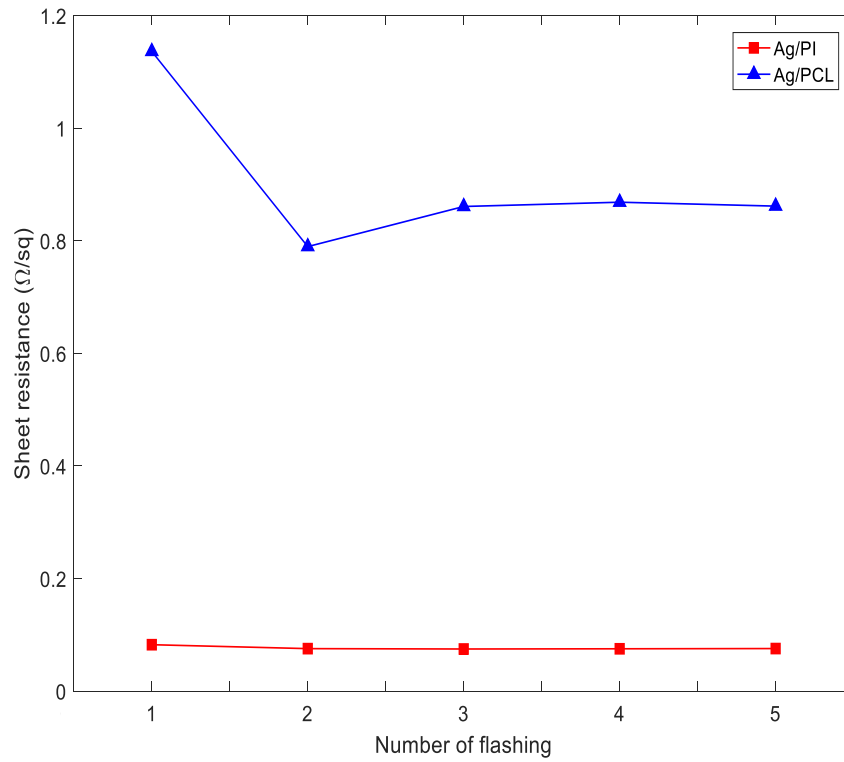


Figure 24. The relationship between electrical resistance and the number of light pulses for inkjet-printed Ag patterns on to PI and PCL substrates

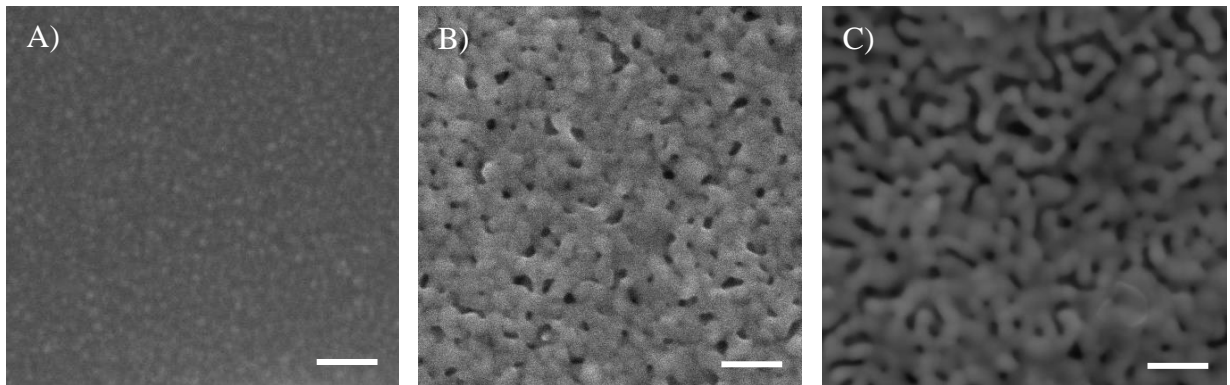


Figure 25. SEM images for Ag nanoparticles: A) before sintering, B) after thermal sintering, and C) after light sintering. The scale bars indicate 100 nm, 250 nm, and 250 nm respectively

5.5 Physiological Recordings

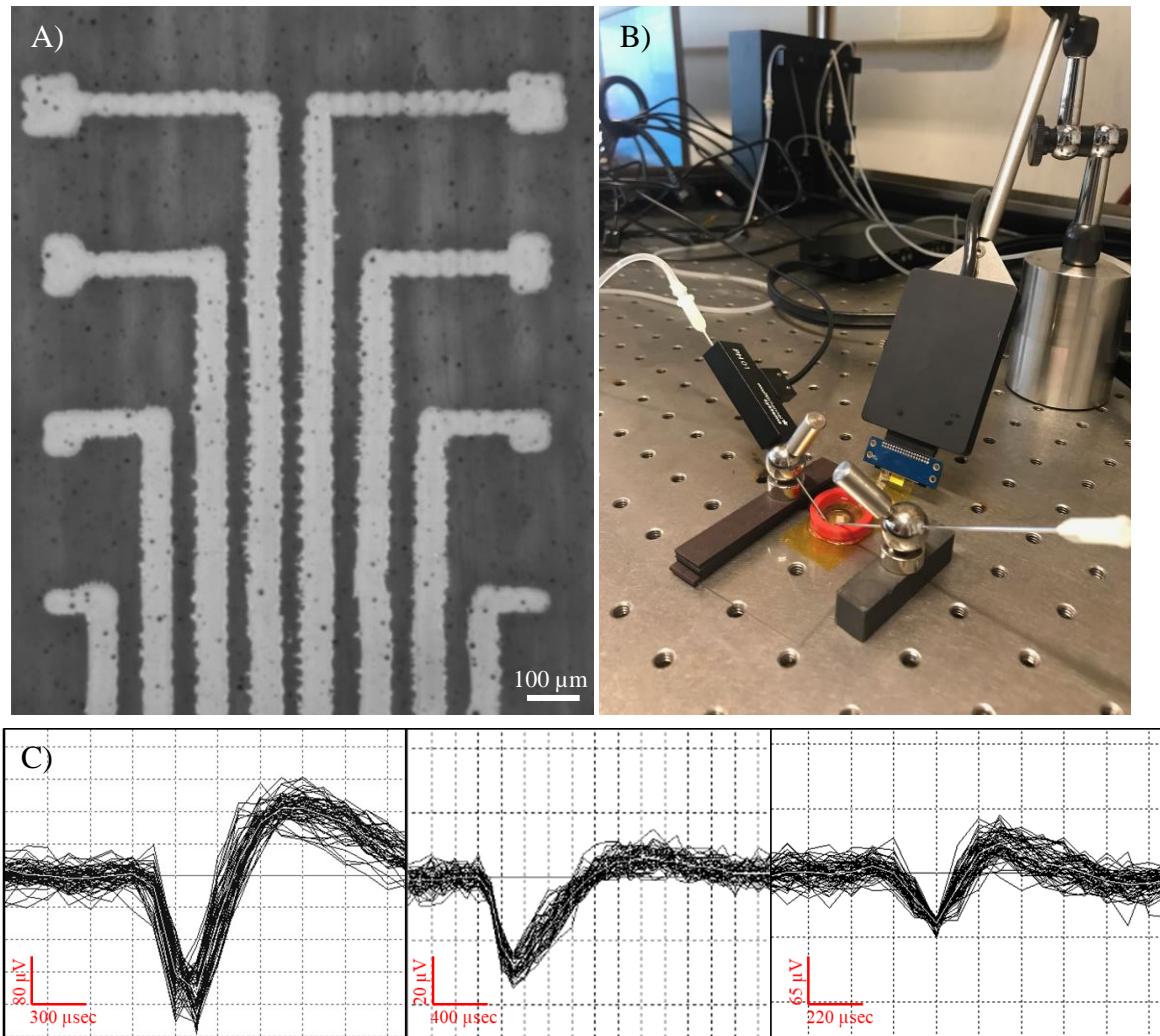


Figure 26. A) A printed array showing 8 electrodes with different diameters ranged between 50 μm to 100 μm . B) Closeup of the recording setup where the array in (A) is connected to the ME2100 system via zifboard. C) Three single-units activity recorded by electrodes array and detected by spike sorter

The 8-electrode array, shown in figure 26A, was connected to the ME2100 system and has successfully detected the spontaneous activity of single cells through multiple electrodes. However, the spontaneous activity was not observed on all recording sites. Compared to the commercially available MEAs, the detected spikes are superimposed on the baseline noise with an SNR that is quite low which required additional post-

processing of the output signal. The amplitude and waveform detected, suggest that the activity belongs to single unit action potentials generated by the ganglion cells, whether from the cell bodies or the axons. The spikes start with a prominent negative deflection that lasts for $\sim 300 \mu\text{sec}$ followed by a positive deflection that lasts longer $\sim 900 \mu\text{sec}$ (Figure 26C). The waveform and amplitude of the spikes resemble those found in previously reported in vitro studies with similar preparation [91-93]. For light responses experiment, the post stimulus time histogram (PSTH) shown in figure 27 suggests that the highest response rate is found near the stimulus of 0.1 s. Then, the initially high spike rate gradually decreases to a steady state.

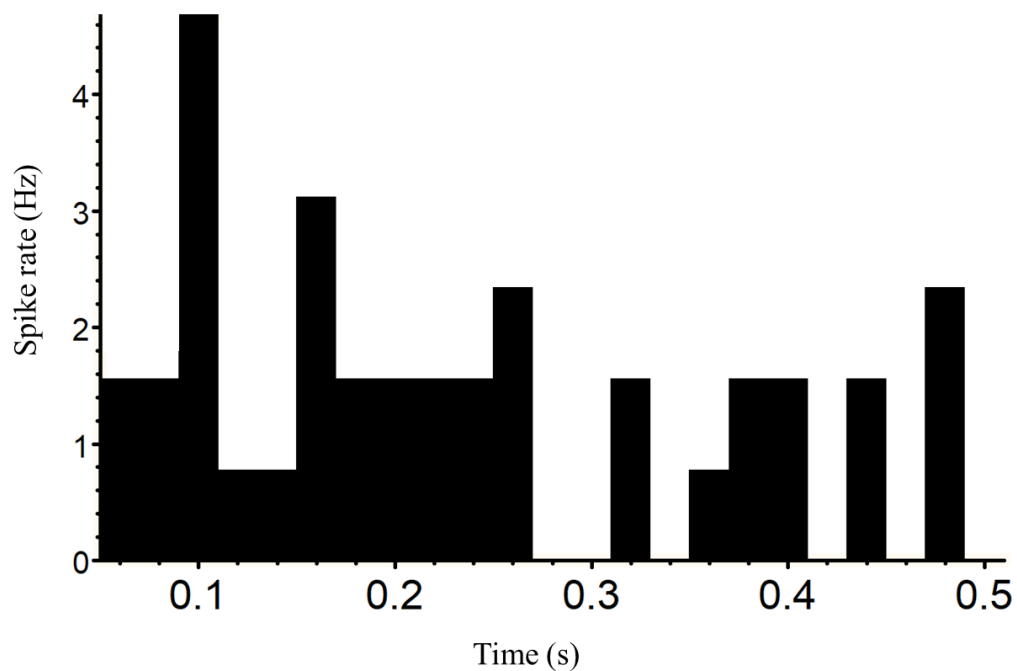


Figure 27. Post stimulus time histogram (PSTH) of a rat retinal ganglion cell response to a light stimulus

5.6 Biocompatibility

The biocompatibility of the chosen substrates was studied *in vitro* using TB assay. The PI substrates showed spreading cells with good adherence and numerous cell-to-cell contact similar to TCP control (Figures 28A and 28D). In contrast, the PCL substrates showed relatively fewer spread cells, where the majority appeared rounded (Figure 28B). However, the spreading cells on the PCL substrates were more stretched and spindle-shaped compared to that on PI and TCP. Beside the rounded cells, it is noted that the PCL substrates had also numerous small clumps of cells. This might be due to the hydrophobic nature of the PCL surface. To induce more favorable adhesion and satisfactory cell responses, it is suggested to add functional groups to the polymer chains, adhesive proteins, or to blend with other hydrophilic degradable polymers [50, 94]. Plasma treatment and coating are other methods to improve the surface characteristics of PCL substrates [94, 95]. In addition, it is observed that the printed arrays (AgNPs and PEDOT:PSS) did not show cytotoxic effects on the cells, where the cells at proximity to the printed patterns were well spread (Figure 28C, white arrows).

After the 72 hours incubation period, TB assay was used. The mean number of viable cells for two independent replicates was calculated. The percentage of viable cells on PCL, PI, and TCP positive control had similar results with 95%, 97%, and 99.5% respectively (Figure 29). The percentage of viable cells on PCL and PI without printed patterns are 96.2% and 98.5% respectively. These results indicate that PI and PCL substrates as well as the printed materials (AgNPs, PEDOT:PSS, and PVPh) are biocompatible and non-toxic. It is worth mentioning that the biocompatibility of PI-based neural implants was previously verified *in vitro* on 3T3 fibroblasts [96]. However, to our knowledge, the biocompatibility of PCL-based neural implants has not been verified yet.

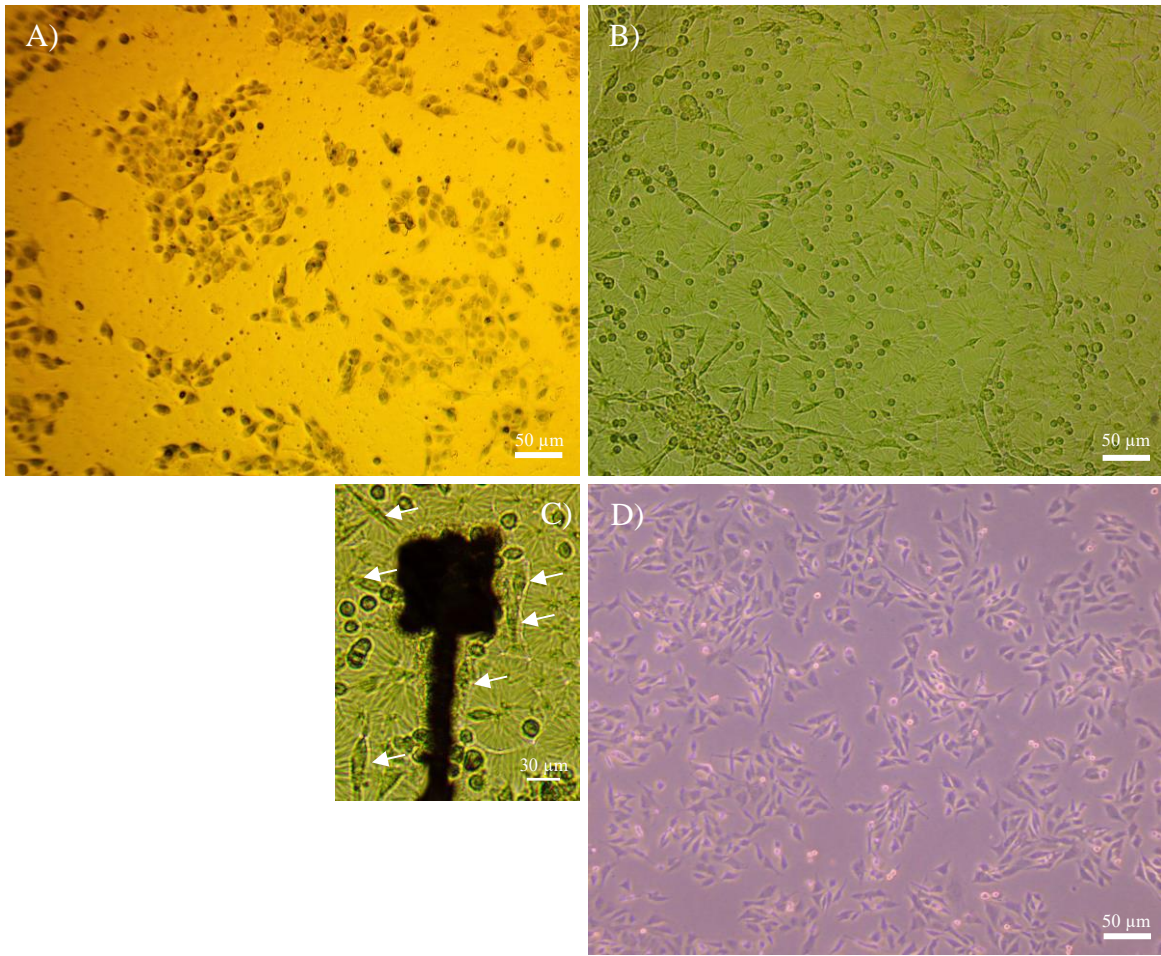


Figure 28. Photomicrographs depicting morphology of adherent PC12 cells on: A) PI substrate, B) PCL substrate, and D) TCP (control). C) Electrode surrounded by PC12 cells on PCL substrate

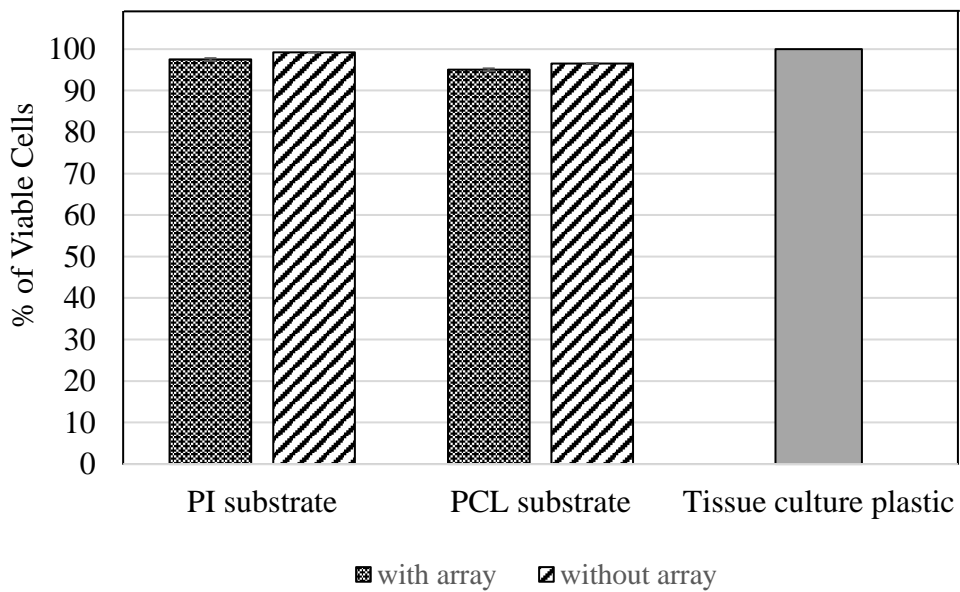


Figure 29. The percentage of viable cells in total cell population on PI substrate, PCL substrate, and tissue culture plastic

5.7 Degradation Test

An accelerated degradation test was successfully conducted to simulate the real-time degradation behavior. PCL/PLGA-based interface's degradation process was used for comparison. Figure 30 shows a series of images taken at several stages of accelerated dissolution in a buffer solution (pH 13) at 37 °C for PCL (A), and PCL/PLGA (B). The PCL-based array degraded within 60 hours and completely disappeared after 70 hours. On the other hand, the blended PCL/PLGA array completely disappeared within less than 60 hours. Therefore, it is concluded that blending PCL with polymers that have faster degradation rate, like PLGA, increases the overall degradation process. It is noted that the part that has the pattern on degrades lastly. It is important to mention that in-vitro degradation in such high pH level is based on chemical hydrolysis only. The presence of enzymes and cells would accelerate the degradation even further. Accordingly, we speculate that the chosen materials and the design of the interface will allow complete degradation in two years. However, in-vivo experiments should be conducted for accurate estimation and confirmation of the degradation rate. Also, the thickness and dimensions of the array influence the degradation time.

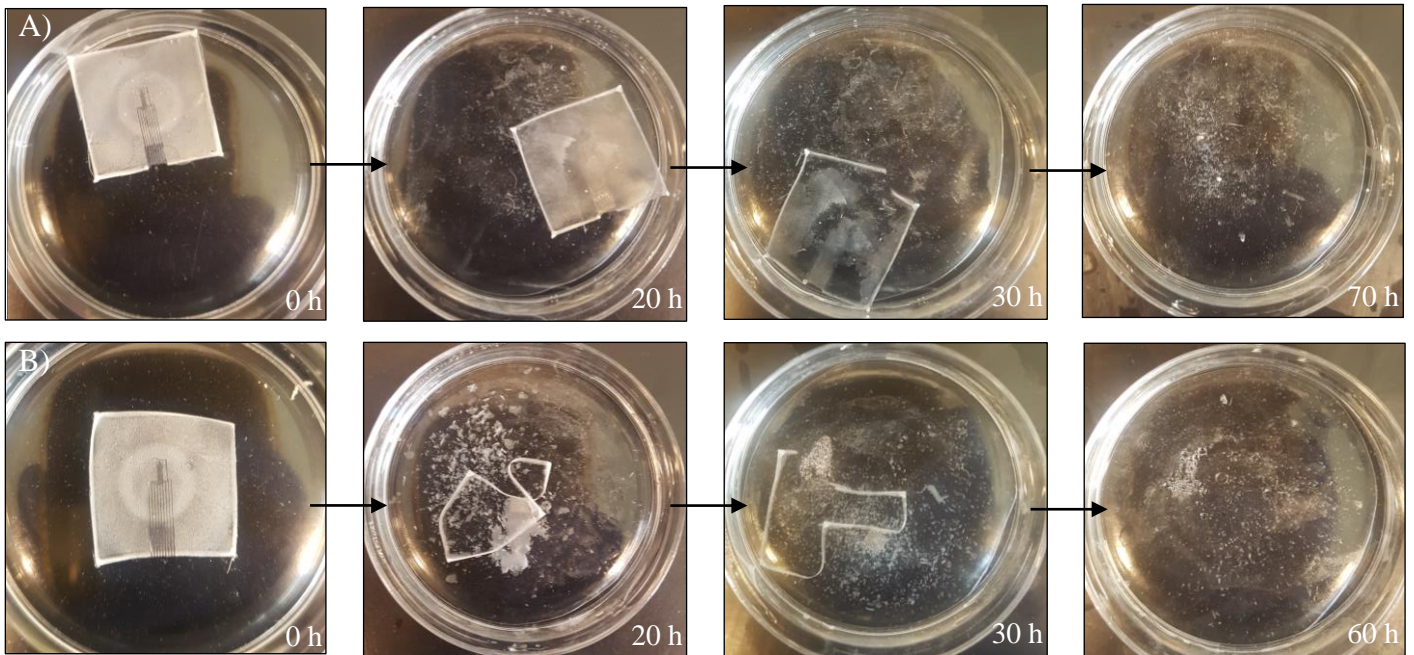


Figure 30. Images collected at several stages of accelerated dissolution of interfaces immersed into an aqueous buffer solution (pH 13) at 37 °C. A) for PCL, and B) for PCL/PLGA

CHAPTER 6

DISCUSSION

Current neural implants are subjected to multiple physiological and mechanical challenges which limit their functional lifespan. High-risk surgical interventions are therefore needed to remove the implant which could cause severe damage to the surrounding tissues as well as inflammation responses. To overcome such challenges, biodegradable soft materials have been proposed to fabricate neural interfaces. Such materials have low melting temperatures, and thus require more complicated steps to eliminate the harsh chemical and thermal fabrication processes. The major technological advances in micro/nano fabrication have facilitated the production of such sophisticated neural interfaces, yet there has been no work that combines soft biodegradable backbones with recording microelectrodes of high electrochemical performance using low-temperature and cost-effective fabrication technique. The primary purpose of our work is to design a biodegradable recording interface that eliminates the need for device resection and exhibits high electrochemical performance in hostile environments via inkjet printing technology. Different biodegradable materials were tested as a potential substrate for our designed array. The flexible PI, which is one of the current state-of-the-art material in the field of implantable devices, was used as a baseline for our work.

Starting with the biodegradable interface, our experiments showed that PCL is a convenient biodegradable material when used as a substrate and an insulator of the designed interface. It showed remarkable mechanical properties, proper stability and biocompatibility in physiological conditions, as well as excellent ink adhesion. The latter

was governed by the roughness and hydrophobic nature of the PCL surface which enables printing well-defined patterns. However, the island-like raises added some challenges to the process of controlling the printing quality. It also slightly affected the spreading and adhesion of cells, compared to PI substrate, without compromising their viability. A solution to such challenge could be heat pressing the PCL film within its melting temperature to smoothen the surface and enhance the printing quality while maintaining its hydrophobic nature. However, pressing duration and temperature used for melting PCL must be precisely adjusted to avoid making a huge change in its mechanical properties.

In addition, our study showed a difference in impedance and CSC values between electrodes printed on PCL substrate and those printed on PI substrate. PCL-based electrodes presented higher impedance and lower CSC values compared to PI-based electrodes which could be due to: 1) The photonic technique that PCL-based electrodes undergo to sinter AgNPs, which possibly alters the electrical properties and the electrochemical performance of the electrodes. Photonic sintering requires adequate control of some parameters like pulse width, number of pulses, duration between pulses, and light-source to substrate distance. All these parameters require sophisticated setup to achieve a satisfactory sintering without any cracks or surface defects, which is not fully provided by a simple camera flashlight; 2) The presence of microstructures on the surface of PCL causes some narrowing and breaking in the connection between the electrode and the circuitry, therefore increasing its resistance. As mentioned earlier, heat pressing the films might solve this problem.

For PI-based array, PVPh was used as the insulation layer. Printing PVPh was a main technical challenge that has restricted the number of channels to 8 electrodes instead

of 16. A widely used organic alcohol (1-hexanol) was utilized as a solvent for PVPh, however, the jetted droplets dry in a non-uniform fashion due to the volatile nature of it. In other words, our lab-prepared ink formulation (PVPh, PMF, and 1-Hexanol) has complicated the process of controlling the uniformity and alignment of the deposited films. On the other hand, other formulations can be prepared using the same polymer ratios but without volatile solvents, such as 1-methyl-2-pyrrolid-inone [97]. In addition, as we increased the drop spacing to better control the deposition of PVPh, pinholes were formed which required printing more layers. To solve this issue, it is suggested to use SU-8 for insulation since a single layer of it provides an improved electrical insulation with better uniformity and alignment accuracy [78, 98]. For better characterization, an optical profilometer can be utilized to assess the thickness and surface features of each insulation material.

Moreover, our results revealed a significant variation in impedance and CSC values between electrodes coated by graphene/PEDOT:PSS and those coated by only PEDOT:PSS. Graphene/PEDOT:PSS coated electrodes performed better, in which a single layer of this material showed low impedance and high CSC values that are equivalent to nearly 7 layers of PEDOT:PSS alone. This could be attributed to the massive increase in the active surface area resulted from graphene micro/nano protrusions covering the surface of the electrode. Furthermore, mixing conductive polymers like PEDOT:PSS with graphene provides additional electrochemical means to the electrodes. Furthermore, multiple layering of coating materials noticeably enhanced the electrochemical performance of the electrodes. This could be explained by the increase in the coating thickness and therefore the total active surface area of the flat electrodes.

Retinal recording results showed a single unit activity from spontaneously firing ganglion cells. It should be noted, however, that the SNR was not comparable to that obtained from commercially available MEAs. In addition, the spikes were not observed on all recording sites. This can be due to the number of channels connected to the system, where the commercial MEAs has 32 channels while our array has only 8 channels. More channels would increase the probability of detecting the neural activity. This can only be achieved by better deposition control of the insulation layer with lower thickness. Another approach for better contact between the electrodes and the neural cells is coating the electrodes with adhesion promoting proteins such as poly-l-lysine. Moreover, the weak connection between the thin array and the zifboard connected to the system may have caused higher SNR. An intermediate or conductive epoxy can be added to tighten the contact and ensure proper connection.

CHAPTER 7

CONCLUSION

In this thesis, new technologies were utilized to fabricate a biodegradable interface with a single-cell resolution for neural recording. The inkjet printing technique for patterning the Ag/PEDOT:PSS electrodes has been optimized to facilitate reliable and enhanced electrochemical performance. This process requires having decent knowledge in material science to enable design freedom for scaling down to micron-resolution with high printing quality. Our work has provided key information on material choices, fabrication processes, and electrophysiological recording. Among other neuro-technologies, the novelty pursued in this thesis is in integrating such single-unit recording interface into a biodegradable substrate through cost effective drop-on-demand deposition. Our results showed that the PCL-based array could serve as a potential candidate for biodegradable and flexible neural implants that can be used in pre-clinical and clinical trials.

A future work would include exploring the ability of the array to record spontaneous activity of neurons, whether from differentiated PC12 neural cells or from the cortical surface of a rat brain. In vivo testing is also required to further prove and show the actual biocompatibility and biodegradable behavior of the interface. In addition, charge injection experiments can be done to test the ability of the electrodes to stimulate the neural activity. Additionally, a wide variety of material inks can be investigated to enhance the design of the interface and provide a higher printing resolution.

The designed interface brings neuro-technology a step closer to improve prosthetic intervention which includes reducing tissue damage and increasing stimulation/recording resolution. The novel use of low-temperature fabrication technique paves the way for using a wide variety of soft biodegradable materials in neural implants.

BIBLIOGRAPHY

1. Vitale, F., et al., *Biomimetic extracellular matrix coatings improve the chronic biocompatibility of microfabricated subdural microelectrode arrays*. PloS one, 2018. **13**(11): p. e0206137.
2. Yu, K.J., et al., *Bioresorbable silicon electronics for transient spatiotemporal mapping of electrical activity from the cerebral cortex*. Nature materials, 2016. **15**(7): p. 782.
3. Cui, Z., *Printed electronics: materials, technologies and applications*. 2016: John Wiley & Sons.
4. Hamill, O.P., et al., *Improved patch-clamp techniques for high-resolution current recording from cells and cell-free membrane patches*. Pflügers Archiv, 1981. **391**(2): p. 85-100.
5. Akaike, N. and N. Harata, *Nystatin perforated patch recording and its applications to analyses of intracellular mechanisms*. The Japanese journal of physiology, 1994. **44**(5): p. 433-473.
6. De Vittorio, M., L. Martiradonna, and J. Assad, *Nanotechnology and neuroscience: nano-electronic, photonic and mechanical neuronal interfacing*. Vol. 8. 2014: Springer.
7. Thomas Jr, C., et al., *A miniature microelectrode array to monitor the bioelectric activity of cultured cells*. Experimental cell research, 1972. **74**(1): p. 61-66.
8. Pine, J., *Recording action potentials from cultured neurons with extracellular microcircuit electrodes*. Journal of neuroscience methods, 1980. **2**(1): p. 19-31.
9. Lin, Z.C., et al., *Iridium oxide nanotube electrodes for sensitive and prolonged intracellular measurement of action potentials*. Nature communications, 2014. **5**: p. 3206.
10. Spira, M.E., et al. *Improved neuronal adhesion to the surface of electronic device by engulfment of protruding micro-nails fabricated on the chip surface*. in *TRANSDUCERS 2007-2007 International Solid-State Sensors, Actuators and Microsystems Conference*. 2007. IEEE.
11. Ryu, M., et al., *Enhancement of interface characteristics of neural probe based on graphene, ZnO nanowires, and conducting polymer PEDOT*. ACS applied materials & interfaces, 2017. **9**(12): p. 10577-10586.
12. Khorrami, M. and M.R. Abidian. *Aligned Conducting Polymer Nanotubes for Neural Prostheses*. in *2018 40th Annual International Conference of the IEEE Engineering in Medicine and Biology Society (EMBC)*. 2018. IEEE.
13. Vosgueritchian, M., D.J. Lipomi, and Z. Bao, *Highly conductive and transparent PEDOT: PSS films with a fluorosurfactant for stretchable and flexible transparent electrodes*. Advanced functional materials, 2012. **22**(2): p. 421-428.
14. Lipomi, D.J., et al., *Electronic properties of transparent conductive films of PEDOT: PSS on stretchable substrates*. Chemistry of Materials, 2012. **24**(2): p. 373-382.
15. Lipomi, D.J. and Z. Bao, *Stretchable, elastic materials and devices for solar energy conversion*. Energy & Environmental Science, 2011. **4**(9): p. 3314-3328.

16. Kim, J., et al., *Enhancement of electrical conductivity of poly (3, 4-ethylenedioxythiophene)/poly (4-styrenesulfonate) by a change of solvents*. Synthetic Metals, 2002. **126**(2-3): p. 311-316.
17. Tevi, T., et al., *Effect of Triton X-100 on the double layer capacitance and conductivity of poly (3, 4-ethylenedioxythiophene): poly (styrenesulfonate)(PEDOT: PSS) films*. Synthetic Metals, 2014. **191**: p. 59-65.
18. Oh, J.Y., et al., *Effect of PEDOT nanofibril networks on the conductivity, flexibility, and coatability of PEDOT: PSS films*. ACS applied materials & interfaces, 2014. **6**(9): p. 6954-6961.
19. Cui, X.T. and D.D. Zhou, *Poly (3, 4-ethylenedioxythiophene) for chronic neural stimulation*. IEEE Transactions on Neural Systems and Rehabilitation Engineering, 2007. **15**(4): p. 502-508.
20. Ludwig, K.A., et al., *Chronic neural recordings using silicon microelectrode arrays electrochemically deposited with a poly (3, 4-ethylenedioxythiophene)(PEDOT) film*. Journal of neural engineering, 2006. **3**(1): p. 59.
21. Wilks, S.J., et al., *Poly (3, 4-ethylene dioxythiophene)(PEDOT) as a micro-neural interface material for electrostimulation*. Frontiers in neuroengineering, 2009. **2**: p. 7.
22. Richardson-Burns, S.M., et al., *Polymerization of the conducting polymer poly (3, 4-ethylenedioxythiophene)(PEDOT) around living neural cells*. Biomaterials, 2007. **28**(8): p. 1539-1552.
23. Cellot, G., et al., *PEDOT: PSS interfaces support the development of neuronal synaptic networks with reduced neuroglia response in vitro*. Frontiers in neuroscience, 2016. **9**: p. 521.
24. Greve, F., et al., *Molecular design and characterization of the neuron–microelectrode array interface*. Biomaterials, 2007. **28**(35): p. 5246-5258.
25. Abidian, M.R. and D.C. Martin, *Multifunctional nanobiomaterials for neural interfaces*. Advanced Functional Materials, 2009. **19**(4): p. 573-585.
26. Cho, K., et al., *Therapeutic nanoparticles for drug delivery in cancer*. Clinical cancer research, 2008. **14**(5): p. 1310-1316.
27. Sahoo, S.K., R. Misra, and S. Parveen, *Nanoparticles: a boon to drug delivery, therapeutics, diagnostics and imaging*, in *Nanomedicine in Cancer*. 2017, Pan Stanford. p. 73-124.
28. Li, G., et al., *Biosensor based on bacterial cellulose-Au nanoparticles electrode modified with laccase for hydroquinone detection*. Colloids and Surfaces A: Physicochemical and Engineering Aspects, 2016. **509**: p. 408-414.
29. Angelina, J.T.T., et al., *Pulsed laser deposition of silver nanoparticles on prosthetic heart valve material to prevent bacterial infection*. Materials Technology, 2017. **32**(3): p. 148-155.
30. Zhang, Z. and W. Zhu, *Controllable synthesis and sintering of silver nanoparticles for inkjet-printed flexible electronics*. Journal of Alloys and Compounds, 2015. **649**: p. 687-693.
31. Lee, C., et al., *Cu-Ag core–shell nanoparticles with enhanced oxidation stability for printed electronics*. Nanotechnology, 2015. **26**(45): p. 455601.

32. Shanmuga Sundari, I. and K. Vithiya, *Developments and Applications of Silver Nanoparticles in the Nutraceuticals Industry*, in *Nanotechnology in Nutraceuticals*. 2016, CRC Press. p. 139-156.
33. Adabi, M., et al., *Biocompatibility and nanostructured materials: applications in nanomedicine*. Artificial cells, nanomedicine, and biotechnology, 2017. **45**(4): p. 833-842.
34. Hoshyar, N., et al., *The effect of nanoparticle size on in vivo pharmacokinetics and cellular interaction*. Nanomedicine, 2016. **11**(6): p. 673-692.
35. Raza, M., et al., *Size-and shape-dependent antibacterial studies of silver nanoparticles synthesized by wet chemical routes*. Nanomaterials, 2016. **6**(4): p. 74.
36. Milić, M., et al., *Cellular uptake and toxicity effects of silver nanoparticles in mammalian kidney cells*. Journal of Applied Toxicology, 2015. **35**(6): p. 581-592.
37. Yang, L. and D.J. Watts, *Particle surface characteristics may play an important role in phytotoxicity of alumina nanoparticles*. Toxicology letters, 2005. **158**(2): p. 122-132.
38. Martinez-Castanon, G., et al., *Synthesis and antibacterial activity of silver nanoparticles with different sizes*. Journal of Nanoparticle Research, 2008. **10**(8): p. 1343-1348.
39. Greulich, C., et al., *The toxic effect of silver ions and silver nanoparticles towards bacteria and human cells occurs in the same concentration range*. Rsc Advances, 2012. **2**(17): p. 6981-6987.
40. Slotkin, J.R., et al., *Biodegradable scaffolds promote tissue remodeling and functional improvement in non-human primates with acute spinal cord injury*. Biomaterials, 2017. **123**: p. 63-76.
41. Velasco, M.A., C.A. Narváez-Tovar, and D.A. Garzón-Alvarado, *Design, materials, and mechanobiology of biodegradable scaffolds for bone tissue engineering*. BioMed research international, 2015. **2015**.
42. Kozai, T.D., et al., *Chronic tissue response to carboxymethyl cellulose based dissolvable insertion needle for ultra-small neural probes*. Biomaterials, 2014. **35**(34): p. 9255-9268.
43. Alt, M.T., et al., *Let there be light—optoprobes for neural implants*. Proceedings of the IEEE, 2017. **105**(1): p. 101-138.
44. Lewitus, D., et al., *Designing tyrosine-derived polycarbonate polymers for biodegradable regenerative type neural interface capable of neural recording*. IEEE Transactions on Neural Systems and Rehabilitation Engineering, 2011. **19**(2): p. 204-212.
45. Park, T.G., *Degradation of poly (lactic-co-glycolic acid) microspheres: effect of copolymer composition*. Biomaterials, 1995. **16**(15): p. 1123-1130.
46. Yu, K.J., et al., *Bioresorbable silicon electronics for transient spatiotemporal mapping of electrical activity from the cerebral cortex*. Nat Mater, 2016. **15**(7): p. 782-791.
47. Pitt, C., et al., *Aliphatic polyesters. I. The degradation of poly (ϵ - caprolactone) in vivo*. Journal of Applied Polymer Science, 1981. **26**(11): p. 3779-3787.
48. Lam, C.X., et al., *Evaluation of polycaprolactone scaffold degradation for 6 months in vitro and in vivo*. Journal of Biomedical Materials Research Part A: An Official Journal of The Society for Biomaterials, The Japanese Society for

- Biomaterials, and The Australian Society for Biomaterials and the Korean Society for Biomaterials, 2009. **90**(3): p. 906-919.
49. Sun, H., et al., *The in vivo degradation, absorption and excretion of PCL-based implant*. Biomaterials, 2006. **27**(9): p. 1735-1740.
 50. Guarino, V., et al., *Polycaprolactone: Synthesis, properties, and applications*. Encyclopedia of Polymer Science and Technology, 2002: p. 1-36.
 51. Vijayavenkataraman, S., et al., *3D-Printed PCL/rGO Conductive Scaffolds for Peripheral Nerve Injury Repair*. Artif Organs, 2018.
 52. Oh, S.H., et al., *In vitro and in vivo characteristics of PCL scaffolds with pore size gradient fabricated by a centrifugation method*. Biomaterials, 2007. **28**(9): p. 1664-1671.
 53. Martin, C., et al., *Directed nerve regeneration enabled by wirelessly powered electrodes printed on a biodegradable polymer*. Adv Healthc Mater, 2014. **3**(7): p. 1001-6.
 54. Nguyen, H.T., et al., *Electric field stimulation through a biodegradable polypyrrole - co - polycaprolactone substrate enhances neural cell growth*. Journal of Biomedical Materials Research Part A, 2014. **102**(8): p. 2554-2564.
 55. Szarowski, D., et al., *Brain responses to micro-machined silicon devices*. Brain research, 2003. **983**(1-2): p. 23-35.
 56. Turner, C.H., et al., *The elastic properties of trabecular and cortical bone tissues are similar: results from two microscopic measurement techniques*. Journal of biomechanics, 1999. **32**(4): p. 437-441.
 57. Lee, H., et al., *Biomechanical analysis of silicon microelectrode-induced strain in the brain*. Journal of neural engineering, 2005. **2**(4): p. 81.
 58. Hoogerwerf, A.C. and K.D. Wise, *A three-dimensional microelectrode array for chronic neural recording*. IEEE Transactions on Biomedical Engineering, 1994. **41**(12): p. 1136-1146.
 59. Yeager, J.D., et al., *Characterization of flexible ECoG electrode arrays for chronic recording in awake rats*. Journal of neuroscience methods, 2008. **173**(2): p. 279-285.
 60. Hassler, C., T. Boretius, and T. Stieglitz, *Polymers for neural implants*. Journal of Polymer Science Part B: Polymer Physics, 2011. **49**(1): p. 18-33.
 61. Bilston, L.E., *Neural tissue biomechanics*. Vol. 3. 2011: Springer Science & Business Media.
 62. Grubb, P.M., et al., *Inkjet Printing of High Performance Transistors with Micron Order Chemically Set Gaps*. Sci Rep, 2017. **7**(1): p. 1202.
 63. Stieglitz, T., *Development of a micromachined epiretinal vision prosthesis*. Journal of neural engineering, 2009. **6**(6): p. 065005.
 64. Lago, N., et al., *Long term assessment of axonal regeneration through polyimide regenerative electrodes to interface the peripheral nerve*. Biomaterials, 2005. **26**(14): p. 2021-2031.
 65. Navarro, X., et al., *A critical review of interfaces with the peripheral nervous system for the control of neuroprostheses and hybrid bionic systems*. Journal of the Peripheral Nervous System, 2005. **10**(3): p. 229-258.
 66. Boretius, T., et al., *A transverse intrafascicular multichannel electrode (TIME) to interface with the peripheral nerve*. Biosensors and Bioelectronics, 2010. **26**(1): p. 62-69.

67. Rubehn, B., et al., *A MEMS-based flexible multichannel ECoG-electrode array*. Journal of neural engineering, 2009. **6**(3): p. 036003.
68. Rubehn, B. and T. Stieglitz, *In vitro evaluation of the long-term stability of polyimide as a material for neural implants*. Biomaterials, 2010. **31**(13): p. 3449-3458.
69. Basaran, O.A., *Small - scale free surface flows with breakup: Drop formation and emerging applications*. AIChE Journal, 2002. **48**(9): p. 1842-1848.
70. He, Y., et al., *An investigation of the behavior of solvent based polycaprolactone ink for material jetting*. Scientific reports, 2016. **6**: p. 20852.
71. Ainsley, C., N. Reis, and B. Derby, *Freeform fabrication by controlled droplet deposition of powder filled melts*. Journal of materials science, 2002. **37**(15): p. 3155-3161.
72. Dong, H., W.W. Carr, and J.F. Morris, *An experimental study of drop-on-demand drop formation*. Physics of fluids, 2006. **18**(7): p. 072102.
73. Dong, H., W.W. Carr, and J.F. Morris, *Visualization of drop-on-demand inkjet: Drop formation and deposition*. Review of Scientific Instruments, 2006. **77**(8): p. 085101.
74. Khodagholy, D., et al., *NeuroGrid: recording action potentials from the surface of the brain*. Nature neuroscience, 2015. **18**(2): p. 310.
75. Garnett, E. and D. Ginley, *Electrical and morphological properties of inkjet printed pedot/pss films*. Journal of Undergraduate Research, 2005. **5**.
76. Cho, S.R., et al., *Effect of nonionic surfactant additive in PEDOT: PSS on PFO emission layer in organic-inorganic hybrid light-emitting diode*. ACS applied materials & interfaces, 2018. **10**(11): p. 9612-9619.
77. Lopez, M., J. Sanchez, and M. Estrada. *Characterization of PEDOT: PSS dilutions for inkjet printing applied to OLED fabrication*. in *PROCEEDING 7th International Caribbean Conference on Devices, Circuits and Systems, Cancun, Mexico*. 2008.
78. Tehrani, B.K., et al., *Development, characterization, and processing of thin and thick inkjet-printed dielectric films*. Organic Electronics, 2016. **29**: p. 135-141.
79. Hetke, J.F., et al., *Silicon ribbon cables for chronically implantable microelectrode arrays*. IEEE Transactions on Biomedical Engineering, 1994. **41**(4): p. 314-321.
80. Najafi, K., J. Ji, and K. Wise, *Scaling limitations of silicon multichannel recording probes*. IEEE transactions on biomedical engineering, 1990. **37**(1): p. 1-11.
81. Robinson, D.A., *The electrical properties of metal microelectrodes*. Proceedings of the IEEE, 1968. **56**(6): p. 1065-1071.
82. Schroder, K., S. McCool, and W. Furlan, *Broadcast photonic curing of metallic nanoparticle films*. NSTI Nanotech May, 2006. **7**: p. 11.
83. Kang, J.S., et al., *Sintering of Inkjet-Printed Silver Nanoparticles at Room Temperature Using Intense Pulsed Light*. Journal of Electronic Materials, 2011. **40**(11): p. 2268-2277.
84. Yung, K.C., et al., *Ink-jet printing and camera flash sintering of silver tracks on different substrates*. Journal of Materials Processing Technology, 2010. **210**(15): p. 2268-2272.
85. Grouchko, M., et al., *Conductive inks with a "built-in" mechanism that enables sintering at room temperature*. ACS nano, 2011. **5**(4): p. 3354-3359.

86. Cheng, L., et al., *Efficient gene transfer to retinal pigment epithelium cells with long-term expression*. *Retina* (Philadelphia, Pa.), 2005. **25**(2): p. 193.
87. Khraiche, Jackson, and Muthuswamy, *Early Onset of Electrical Activity in Developing Neurons Cultured on Carbon Nanotube Immobilized Microelectrodes*. 2015: p. 1-4.
88. Łapkowski, M. and A. Proń, *Electrochemical oxidation of poly (3, 4-ethylenedioxythiophene)—“in situ” conductivity and spectroscopic investigations*. *Synthetic Metals*, 2000. **110**(1): p. 79-83.
89. Nguyen, T., et al., *Chemical and thermal treatment of PEDOT: PSS thin films for use in organic light emitting diodes*. *Surface and Coatings Technology*, 2004. **180**: p. 646-649.
90. Chung, W.H., et al., *In situ monitoring of a flash light sintering process using silver nano-ink for producing flexible electronics*. *Nanotechnology*, 2013. **24**(3): p. 035202.
91. Kuffler, S.W., *Discharge patterns and functional organization of mammalian retina*. *Journal of neurophysiology*, 1953. **16**(1): p. 37-68.
92. Meister, M., J. Pine, and D.A. Baylor, *Multi-neuronal signals from the retina: acquisition and analysis*. *Journal of neuroscience methods*, 1994. **51**(1): p. 95-106.
93. Grumet, A.E., J.L. Wyatt Jr, and J.F. Rizzo III, *Multi-electrode stimulation and recording in the isolated retina*. *Journal of neuroscience methods*, 2000. **101**(1): p. 31-42.
94. Siri, S., et al., *Surface modification of electrospun PCL scaffolds by plasma treatment and addition of adhesive protein to promote fibroblast cell adhesion*. *Materials Science and Technology*, 2010. **26**(11): p. 1292-1297.
95. Yan, D., et al., *Plasma treatment of electrospun PCL random nanofiber meshes (NFMs) for biological property improvement*. *Journal of Biomedical Materials Research Part A*, 2013. **101**(4): p. 963-972.
96. Lee, K., et al., *Polyimide based neural implants with stiffness improvement*. *Sensors and Actuators B: Chemical*, 2004. **102**(1): p. 67-72.
97. Chen, B., et al., *All-polymer RC filter circuits fabricated with inkjet printing technology*. *Solid-State Electronics*, 2003. **47**(5): p. 841-847.
98. Cook, B.S., J.R. Cooper, and M.M. Tentzeris, *Multi-layer RF capacitors on flexible substrates utilizing inkjet printed dielectric polymers*. *IEEE Microwave and Wireless Components Letters*, 2013. **23**(7): p. 353-355.

